Monthly Notices
of the
ROYAL ASTRONOMICAL SOCIETY

MNRAS **462,** 362–381 (2016)
Advance Access publication 2016 July 19

doi:10.1093/mnras/stw1676

Common envelope events with low-mass giants: understanding the transition to the slow spiral-in

N. Ivanova[1]★ and J. L. A. Nandez[1,2]

[1] *University of Alberta, Edmonton, AB, T6G 2R3, Canada*
[2] *SHARCNET, The University of Western Ontario London, Ontario, N6A 5B7, Canada*

Accepted 2016 July 11. Received 2016 July 8; in original form 2015 November 23

ABSTRACT

We present a three-dimensional (3D) study of common envelope events (CEEs) to provide a foundation for future one-dimensional (1D) methods to model the self-regulated phase of a CEE. The considered CEEs with a low-mass red giant end with one of three different outcomes – merger, slow spiral-in, or prompt formation of a binary. To understand which physical processes determine different outcomes, and to evaluate how well 1D simulations model the self-regulated phase of a CEE, we introduce tools that map our 3D models to 1D profiles. We discuss the differences in the angular momentum and energy redistribution in 1D and 3D codes. We identified four types of ejection processes: the pre-plunge-in ejection, the outflow during the plunge-in, the outflow driven by recombination, and the ejection triggered by a contraction of the circum-binary envelope. Significant mass is lost in all cases, including the mergers. Therefore, a self-regulated spiral-in can start only with a strongly reduced envelope mass. We derive the condition to start a recombination outflow, which can proceed either as a runaway or a stationary outflow. We show that the way the energy of the inspiralling companion is added to the envelope in 1D studies intensifies the envelope's entropy increase, alters the start of the recombination outflow, and leads to different outcomes in 1D and 3D studies. The steady recombination outflow may dispel most of the envelope in all slow spiral-in cases, making the existence of a long-term self-regulated phase debatable, at least for low-mass giant donors.

Key words: hydrodynamics – methods: numerical – binaries: close.

1 INTRODUCTION

A common envelope event (CEE) is an episode in the life of a binary system during which the outer layers of one of the stars expand to engulf the companion – thus producing an envelope around both stars, or a common envelope (CE). The concept was originally proposed almost 40 yr ago by Paczynski (1976) (this publication cites private communication with Ostriker as well as Webbink 1975, for the origin of this idea). The concept was later developed into the modern state of the energy formalism in Webbink (1984) and Livio & Soker (1988). This brief but crucial episode leads either to a complete merger, or to the expulsion of the CE, leaving a drastically shrunk (short-period) binary – a likely future gravitational wave source, or X-ray source, or SN Ia progenitor, etc. The merged star can form a variety of exotic objects, or produce a long gamma-ray burst, one of the most luminous events known to occur in the Universe (for a recent review on the current understanding of the CE, as well as overall importance for binary populations and applications, see Ivanova et al. 2013a). It is widely accepted that a CEE is the *main mechanism* by which an initially wide binary star is converted into a very close binary star, or by which two stars merge.

Despite being vital for understanding a vast number of important binary systems, CEE theory is presently very poorly understood. Brute-force numerical simulations of CEEs are hard (Rasio & Livio 1996; Sandquist et al. 1998; Passy et al. 2012; Ricker & Taam 2012; Nandez, Ivanova & Lombardi 2014, 2015; Ohlmann et al. 2016); often, key elements of the event proceed not only on a dynamical time-scale, but also on a thousand to million times longer thermal time-scale. Various physical processes including radiation transfer, convective energy transport and nuclear burning can take place during a CEE (Ivanova et al. 2013a). Understanding the transition between a fast CEE that can only be modelled using a three-dimensional (3D) hydrodynamical code with simplified physics, and a slow CEE that can only be modelled with a one-dimensional (1D) stellar code, where various mechanisms for the energy transport, nuclear energy generation and other physics are included, was advocated to be the most important step for further progress in CEE studies (Ivanova et al. 2013a). Several research groups have recently restarted to carry out 1D studies of slow CEEs (e.g. Luan &

★ E-mail: nata.ivanova@ualberta.ca

Phinney 2011; Hall 2015; Lopez-Canelas & Politano 2015; Menon & Heger 2015, also Podsiadlowski, private communication). Determining or constraining the initial conditions for 1D CEEs, starting from the moment when the dynamical phase ended, is crucially needed. In addition, 1D simulations, starting from the pioneers (Taam, Bodenheimer & Ostriker 1978; Meyer & Meyer-Hofmeister 1979), are naturally forced to use either assumptions or prescriptions, which have not yet been verified against 3D simulations. For example, prescriptions for the angular momentum transfer or its distribution, or how the released orbital energy is deposited in the envelope.

Understanding the initial conditions at the start of the slow spiral-in, however, cannot be done without understanding how the dynamical phases proceeded: how the energy redistribution between the orbit and the envelope takes place in 3D, as compared to what 1D treatments we adopt, whether any envelope material was lost prior the slow spiral-in, and how important quantities (e.g. specific angular momentum and entropy of the material) have evolved by the end of the rapid evolution.

In this paper, we study the transition to the slow spiral-in by analysing 3D simulations of CEEs with a low-mass giant donor and companions of several different masses. The outcomes of those CEEs vary from a rapid and complete envelope ejection to the strong binary shrinkage that can be indicative of a merger (Section 2). We are most interested in understanding the start of the intermediate regime, when the binary orbital dissipation is not dynamical anymore, but the envelope has not yet been ejected – the regime that 1D codes are best suited to model.

To provide a transition between our results and 1D simulations, we discuss several ways to map the 3D CEE simulations to 1D (Section 3). We compare the results of this mapping with the results of the simplified assumptions and prescriptions that 1D codes have used to study slow CEEs. We also use our mapped simulations to analyse the physical processes during a transition to a slow spiral-in, to find clues about what leads to the branching of the outcomes of CEEs, to consider how strong the asymmetry of the CE at the start of a slow CEE is, and to discuss the challenge with density inversion that a 1D approach may have.

We provide a detailed technical description of how energies are considered in the 1D and 3D approaches (Section 4). This leads to a discussion of how the two kinds of energies can be compared between the approaches and whether the simplified prescription is valid during the transition from fast to the slow spiral-in. We also provide an equation, and its limitations, for how energy conservation should be used in the 1D approach after the start of the slow spiral-in. We analyse the angular momentum redistribution in 3D simulations and compared the results to existing 1D approaches (Section 5).

We discuss in Section 6 how entropy generation is different between the 3D and 1D approaches. We argue that the currently used 1D treatments of energy conservation via 'heating' lead to a different outcome compared to 3D simulations. In particular, the usual 1D treatment leads to a different entropy profile at the start of the slow spiral-in. We discuss next how recombination governs the CE ejecta (Section 7). We then advocate that artificially forced entropy generation, coupled with recombination, may produce unrealistic outcomes in 1D codes. Finally, we consider the ejecta, identify several types of ejecta at various CEE phases, and discuss the physics behind each type of ejecta (Section 8). We conclude with several recommendations for 1D codes that can improve the modelling of CEEs in 1D (Section 9).

2 CLASSIFICATION OF CEE OUTCOMES

2.1 Definitions of CEE phases

In this paper, we adopt the definitions of the distinct phases of a CEE as described by Podsiadlowski (2001), see also the thorough details in the review by Ivanova et al. (2013a). For a more *quantitative* differentiation of the phases, we indicate here the typical rates of the orbital dissipation.

(I) Loss of corotation: during this phase, the change in the orbital separation a is less than one per cent over the orbital period $P_{\rm orb}$, $|(\dot{a}\,P_{\rm orb})|/a < 0.01$. The companion orbits either outside of the future CE, or inside the CE's outer expanded and rarefied layers.

(II) Plunge-in: this is the fastest phase of the orbital shrinkage, when the rate of change of the orbital separation is large, $|(\dot{a}\,P_{\rm orb})|/a \gtrsim 0.1$. The companion plunges inside the CE, and, at the end of the phase, most of the CE mass is outside the companion's orbit. During the plunge-in, the concept of a Keplerian binary orbit is equivocal.

(III) Self-regulating spiral-in: during this stage, the change in the orbital energy $E_{\rm orb}$ is small, $|(\dot{E}_{\rm orb}\,P_{\rm orb})/E_{\rm orb}| < 0.01$. The companion orbits inside the CE.

With a 3D code, a proper self-regulating regime is not possible to achieve – a 3D code typically lacks consideration of energy transport that operates on a thermal time-scale (e.g. convection, see also the recent steps in the treatment of convective envelopes in Ohlmann et al. 2016), among other effects. Therefore, in this paper, we will rather consider the *initial phase* of the self-regulating spiral-in, to which we will refer here as the 'slow spiral-in'.

We define that the slow spiral-in starts with a similar criterion as the self-regulating spiral-in, i.e. when $|(\dot{E}_{\rm orb}\,P_{\rm orb})/E_{\rm orb}| < 0.01$. In our simulations, this stage is modelled for the first few dynamical time-scales of the expanded envelope after the plunge-in has ended. On the other hand, its duration can be compared to about several thousands orbital periods of the formed close binary. A well-established slow spiral-in – thousands binary orbits after the start of the slow spiral-in – could be quite different from the start of the slow spiral-in for the region around the binary. This is because this region's dynamical time-scale is comparable to the binary period, but has evolved for many thousands of the binary periods. On the other hand, it is still in the initial phase of the self-regulated spiral-in as the modelled time is smaller than the thermal time-scale of the envelope.

For the definition of phase III above (as well as for the slow spiral-in), we use the orbital energy dissipation as an indicator, rather than the orbital separation decrease. This is because in our code during this period, the orbital energy of the now close binary is nearly constant, as expected, but the binary has a non-zero, albeit small, eccentricity, and the decrease of its average orbital separation is harder to obtain numerically. Note that due to the adopted quantitative classification of the principal phases as described above, there are also transitional phases: between the end of the corotation and the start of the plunge-in, and between the end of the plunge-in and the start of the slow spiral-in.

2.2 Numerical setup of simulations

To study a CEE from before the Roche lobe (RL) overflow and to a well-established slow spiral-in, we use STARSMASHER, a smoothed particle hydrodynamics (SPH) 3D code (see instrument papers Lombardi et al. 2006, 2011; Gaburov, Lombardi & Portegies

Zwart 2010; Lombardi et al. 2011, where the method and relevant tests are described in detail). An SPH approach is appropriate to model the interaction between two stars without imposing boundary conditions, and is commonly used in the community for this class of problems (e.g. see various implementations used in Davies et al. 1993; Rasio & Livio 1996; Church et al. 2009; Passy et al. 2012). The code STARSMASHER was originally developed to treat interactions between two stars, and has been frequently used in studies of this class of problems (Gaburov et al. 2010; Ivanova et al. 2010; Antonini, Lombardi & Merritt 2011; Lombardi et al. 2011; Nandez et al. 2014, 2015; Hwang et al. 2015; Perets et al. 2016). As an example, one of STARSMASHER's important features, developed specifically for studies of binaries, is the specially designed relaxation setup of a close-to-contact binary (Lombardi et al. 2011). This relaxation procedure minimizes spurious effects of artificial viscosity that may affect the start of the spiral-in.

STARSMASHER's internal physics has been recently upgraded to take into account recombination processes (Nandez et al. 2015). The modification was done by replacing the code's default equation of state that includes ideal gas and radiation pressure (Lombardi et al. 2006) by the tabulated equation of state from MESA that accounts for states of ionization (Paxton et al. 2011, also see more details on which elements are taken into account for recombination in Section 7). The version of SPH code we use evolves specific internal energy of an SPH particle u_i and density of an SPH particle ρ_i (see equations A18 and A7 of Gaburov et al. 2010), and pressure then is found from the internal energy, density, and the adopted equation of state. It is this implementation of the more complete equation of state that has enabled modelling of the complete CE ejection, for the first time.

For this study of the branching of CEE outcomes, we chose for a donor a low-mass red giant with a mass of $1.8\,M_\odot$, a core mass of $0.318\,M_\odot$, and radius $16.3\,R_\odot$ (for more details on the ambiguity in the definition of the donor radius in 3D, see the discussion in Nandez et al. 2014). To create the initial red giant donor star, we use the TWIN/EV stellar code (Eggleton 1971, 1972, recent updates are described in Glebbeek, Pols & Hurley 2008).

To obtain different categories of CEE outcomes, we varied the mass of the companion, $M_{\rm comp}$, considering 0.36, 0.20, 0.15, 0.10 and $0.05\,M_\odot$ companions. At the start of the simulations, donors in all binaries are within their RLs. We consider the case of non-synchronized donors. While synchronization has a small effect on the outcomes (for a discussion of how small the effect of synchronization on the outcomes is, and that it mainly affects the energy carried away by the ejecta, see Nandez et al. 2014), we chose to start with non-synchronized binaries as it significantly speeds up the start of the interaction.

The red giant envelope is modelled with 10^5 particles. The red giant core and the companions are modelled as point masses, where a point mass only interacts gravitationally with normal SPH particles. Such point masses are also referred to as special particles. In an SPH code, the gravitational potential equation contains an extra smoothing term: the smoothing length h_i (see the appendix of Hernquist & Katz 1989). In our simulations, for 10^5 particles, a smoothing length for the red giant core is $0.35\,R_\odot$ (for details on how the smoothing length is determined for special particles in STARSMASHER, see Lombardi et al. 2011).

In previous studies, a larger number of particles has been used to represent the donor (e.g. in Passy et al. 2012, a CEE was modelled using five times more SPH particles). However, the modelled *phase* of a CEE was substantially shorter. For example, Passy et al. (2012) have started their simulations with placing the companion on the surface of the donor, and have finished their simulations at the moment that we define as the start of the slow spiral-in. A similar phase in our simulations takes only between 1 and 2 per cent of the computational time. About 10 per cent of the computational time is spent before the plunge-in starts, and about 90 per cent of the computational time is spent after the plunge-in, until the slow spiral-in is 'well-established.' The simulations take on average 5×10^6 time-step integrations. This allows us to follow about 15 000–35 000 binary periods after the end of the plunge-in. The physical time-scale of the simulations is about 1000 d. While it would be great to model a donor at better resolution, it is not computationally feasible yet to get both a long-term evolution of a CEE, and model it with a resolution substantially larger than 10^5.

The resolution test for STARSMASHER with the original equation of state was performed by Hwang et al. (2015). As compared to that version of the code, only the equation of state has been changed. Nandez et al. (2015) carried out STARSMASHER CEE simulations with 10^5 and 2×10^5 particles in an attempt to test resolution effects. The two simulations were done for the version of the code that includes the recombination physics. The test has shown that the final orbital separation varies by only a few per cent and that both simulations produce a similar envelope ejection (the ejected mass, the time-scale of the ejection, etc.). While doubling resolution is not sufficient to thoroughly test convergence, this is the most that can be achieved at present.[1] This test suggests that most phenomena that are discussed in this manuscript are not likely to be rebutted by a larger resolution run. We warn, however, that some results presented in this paper should be taken with caution, as future studies made with a substantially larger resolution may negate the phenomenon that is produced by a small number of particles – specifically, the shell-triggered ejection discussed later in Section 8.

The orbital energies and the total energies of the CE systems for each companion at the start of the simulations are shown in Table 1. The donor's envelope has an initial total binding energy -4.4×10^{47} erg, an initial potential energy -8.8×10^{47} erg, an initial thermal energy 4.4×10^{47} erg (without recombination energy), and additionally, 4.7×10^{46} erg is stored as recombination energy (see more details on how the recombination energy is found in Section 7).

We distinguish the unbound envelope material, $M_{\rm ej}$, and the currently bound envelope material, $M_{\rm env}$. These masses are found using the technique described in Nandez et al. (2014). Principally, if an SPH particle has negative total energy, it is bound. If an SPH particle has positive total energy, it is unbound and belongs to the ejecta. In Table 1, we provide the final values at the end of the simulations, but note that the mass of the ejecta cannot be simply explained with one number, and more details about the ejecta will be given in Section 8.

During a CEE, a CE system can be described in terms of various energies: the binding energy of the envelope $E_{\rm bind,env}$, the internal energy of the envelope $U_{\rm in,env}$, the thermal energy of the envelope $E_{\rm th,env}$, the recombination energy of the envelope $E_{\rm rec,env}$, the potential energy of the envelope $E_{\rm pot,env}$, the kinetic energy of the envelope

[1] A run with 8×10^5 particles would require 8–10 GPU yr with NVIDIA driver M2070, as was tested. The use of K40, which is currently the fastest NVIDIA driver in the world, would reduce GPU time by 25 per cent. Given the low communication speed between the GPU nodes (hardware limitation, and thus the scaling is only effective up to 4 GPUs and 16 CPUs), and the cumbersome queue setup, this run would require more than 2 yr of waiting time in the real world, if started at the available Westgrid GPU clusters.

Table 1. $M_{\rm comp}$ is the mass of the companion. $E^{\rm ini}_{\rm tot,CE}$, $E^{\rm ini}_{\rm orb,3D}$, $E^{\rm fin}_{\rm orb,3D}$ are the initial total energy of the CE system, the initial orbital energy and the final orbital energy, respectively (for details on definitions, see Section 4.2). $E_{\rm tot,ej}$ is the total energy carried away by the ejecta. $J_{\rm tot}$ and $J_{\rm ej}$ are the total angular momentum and the angular momentum of the ejecta. $a_{\rm orb,fin}$ is the final orbital separation. $M_{\rm env}$, and $M_{\rm unb}$ are the envelope mass and the ejecta, respectively. All the masses are in $\rm M_\odot$, the orbital separation is in $\rm R_\odot$, all the energies are in 10^{46} erg, and all the angular momentums are in 10^{51} g cm^2 s^{-1}. The instants of time for which the final values, including all the quantities for the ejecta, are calculated are either when the separation had decreased to 0.15 $\rm R_\odot$ (for M05 and M10 models), or 50 d after the plunge-in (SS15, SS20 and BF36 models). In addition, for BF36 we also list the values after the entire envelope was ejected (BF36ej). All the models are for the same red giant donor with a mass of 1.8 $\rm M_\odot$ and with a core mass of 0.318 $\rm M_\odot$.

Model	$M_{\rm comp}$	$E^{\rm ini}_{\rm tot,CE}$	$E^{\rm ini}_{\rm orb,3D}$	$E^{\rm fin}_{\rm orb,3D}$	$E^{\rm fin}_{\rm tot,ej}$	$J_{\rm tot}$	$J^{\rm fin}_{\rm ej}$	$a^{\rm fin}_{\rm orb}$	$M^{\rm fin}_{\rm env}$	$M^{\rm fin}_{\rm ej}$
M05	0.05	−40.19	−1.40	−15.75	1.07	1.98	0.34	0.15	1.45	0.02
M10	0.10	−40.79	−1.30	−36.72	4.22	4.05	1.30	0.15	1.18	0.30
SS15	0.15	−41.35	−1.85	−43.88	6.77	6.14	3.48	0.19	1.05	0.43
SS20	0.20	−41.87	−2.38	−46.26	6.90	8.24	5.46	0.29	0.93	0.56
BF36	0.36	−43.40	−3.91	−51.22	9.51	14.93	10.77	0.50	0.67	0.81
BF36ej	0.36	−43.40	−3.91	−52.87	9.64	14.93	13.82	0.48	0.0	1.48

$E_{\rm kin,env}$, the orbital energy of the binary $E_{\rm orb}$, the total energy of the ejecta $E_{\rm tot,ej}$, and the kinetic energy of the ejecta $E_{\rm kin,ej}$. We can also trace the angular momentum of the envelope $J_{\rm env}$, the orbital angular momentum of the binary $J_{\rm orb}$, and the angular momentum of the ejecta $J_{\rm ej}$. Details of how those quantities are obtained from our 3D simulations can be found in Section 4.2 and Appendix A. Values of the most important quantities at the start and the end of each simulation can be found in Table 1. Note that in Table 1, energies have the index '3D', as they are obtained assuming 3D energy definitions (see Section 4.2), and can be different from those inferred by the definitions of the 1D approach (see Section 4.1). We clarify that in all our simulations presented in this paper, the total angular momentum and the total energy are conserved (the error on energy conservation is less than 0.1 per cent of the initial total energy, and the error on angular momentum conservation is less than 0.001 per cent of the initial total angular momentum).

2.3 CEE outcomes

We classify the outcomes of our 3D simulations of CEEs as follows.

(i) Binary formation – if the CE is ejected and $|(\dot{E}_{\rm orb}\,P_{\rm orb})/E_{\rm orb}| < 0.01$.

(ii) Slow spiral-in – if the CE has not been fully ejected and no further rapid mass outflow of the envelope material is taking place on a time-scale longer than a few dynamical time-scales of the expanded CE (although, see Section 8 about the shell-triggered ejecta). During this stage, the orbital energy release is decreased to $|(\dot{E}_{\rm orb}\,P_{\rm orb})/E_{\rm orb}| < 0.01$.

(iii) Merger – if the orbital separation is $<0.15\,\rm R_\odot$ (see discussion below on the ambiguity of a merger case).

In Fig. 1, we show the evolution of the orbital separation for all cases. We have obtained all three possible outcomes: mergers (with companions of mass 0.05 and 0.1 $\rm M_\odot$), slow spiral-ins (with companions of mass 0.15 and 0.2 $\rm M_\odot$) and binary formation (0.36 $\rm M_\odot$ companion). The quantities that describe the simulations are shown in Table 1. We provide these values when the separation becomes 0.15 $\rm R_\odot$, or at 50 d after the end of the plunge-in. For the binary formation case, we also list in Table 1 values for when the entire envelope is lost (about 700 d after the plunge-in has ended).

We also indicate in Fig. 1 the start of the plunge-in, the end of the plunge-in, and the start of the slow spiral-in for all the cases. For example, in the simulation with a 0.15 $\rm M_\odot$ companion, at the end of the plunge-in – when the orbital separation stops changing quickly – the binary separation is about three times larger than during the 'well-established' slow spiral-in (50 d after the end of the plunge-in), and is about two times larger than at the start of the slow spiral-in. The transition between the end of the plunge-in and the start of the slow spiral-in lasts for only about 3 d, which is none the less about 100 binary orbits. It takes another 400 binary orbits before the orbital decay decreases to $|(\dot{E}_{\rm orb}\,P_{\rm orb})/E_{\rm orb}| \sim 10^{-4}$. At about 50 d after the end of the plunge-in, or after about 3000 binary orbits, $|(\dot{E}_{\rm orb}\,P_{\rm orb})/E_{\rm orb}| \sim 10^{-5}$.

For the case when the '*binary formation*' occurs in the simulation, half of the envelope is ejected soon after the end of the plunge-in (on day 374 after the start of the simulation), and it takes about 700 more days to steadily eject the rest of the envelope. We note that before the envelope is fully ejected, this 'binary formation' case is not substantially different from the other two cases that we designate here as '*slow spiral-in*' cases, except for the fact that the CEE evolution is faster with the 0.36 $\rm M_\odot$ companion.

We call a '*merger*' all simulated systems for which the geometrical separation between the core and the companion is $\lesssim$0.15 $\rm R_\odot$. For a non-degenerate companion, this limit on mergers is naturally consistent with the radii of very low-mass stars. For a degenerate companion, technically, the simulations can be forced to run until the separation becomes $\lesssim$0.01 $\rm R_\odot$. However, there are other reasons to stop the simulation earlier. In an SPH code, if the distance between the two point masses is less than two times their smoothing lengths, then there is an extra smoothing in the gravitational potential equation (see, e.g. Hernquist & Katz 1989). Then the orbital energy is not the same as would be found from their geometrical separation. In addition, the orbital energy depends also on the presence of the usual SPH particles within the RLs of the special particles (see below Section 4.2 for more details). Note that these effects take place while the total energy is conserved; the portions of the energy assigned to the binary, and to the envelope, become dependent on the smoothing length. We find that a noticeable (about a few per cent) mismatch between the geometric orbital separation and the 'energy'-derived orbital separation starts to appear when the distance between the special particles is less than $\sim$0.15 $\rm R_\odot$ (see also detailed discussion on this in Nandez & Ivanova 2016).

Accordingly, the potential energy (by its absolute value) is not as large as would be calculated purely by the distance between the particles, if a Keplerian orbit were assumed. As we have checked, decreasing the smoothing length by a factor of 2 and increasing the number of particles by a factor of 8 improves the consistency, but leads to an increase of the computational time by a factor of 64. This makes the problem currently computationally unfeasible. The CEEs with the companions of 0.05 and 0.1 $\rm M_\odot$ have therefore

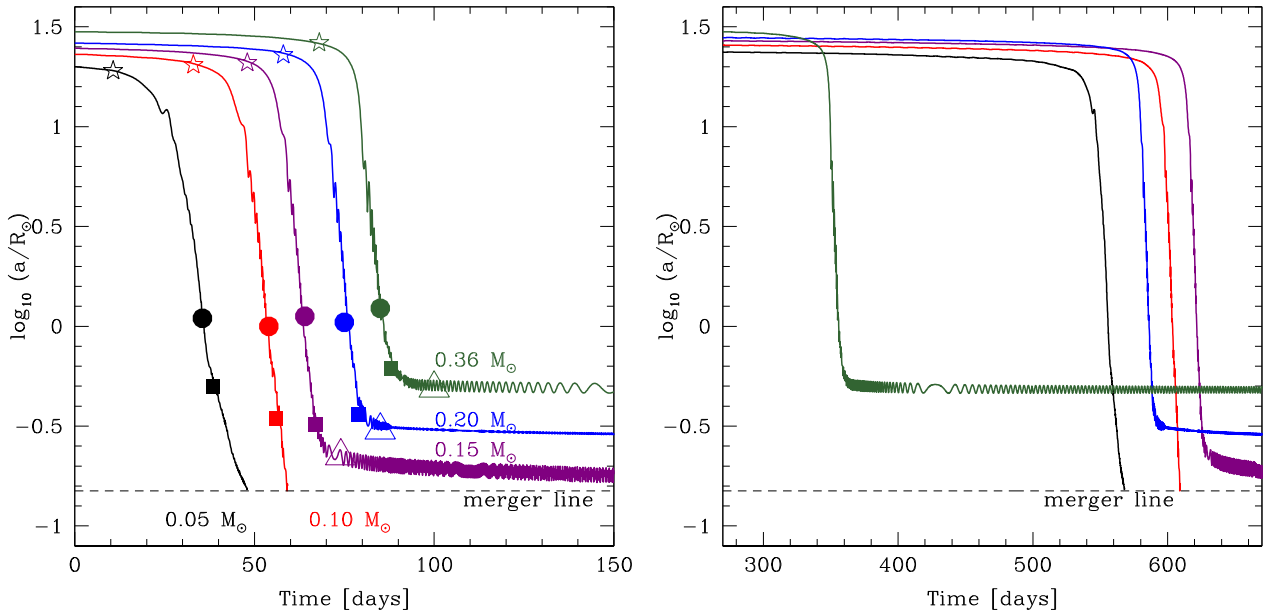

Figure 1. Evolution of orbital separations in the binaries with 0.05, 0.10, 0.15, 0.20, and 0.36 $M_\odot$ companions. On the left-hand panel, the time axis is shifted to show the relative orbital evolution in more detail for each system. The time shifts are 520, 550, 558, 510, and 270 d for 0.05, 0.10, 0.15, 0.20, and 0.36 $M_\odot$ companions, respectively. On the right-hand panel, the time axis is not shifted. Please note that the time that has passed from the start of the simulation to the start of the plunge-in depends strongly on the degree of the initial Roche lobe underflow, and that quantity is slightly different in the simulations. The dashed line indicates where the companion and the red giant core will definitely merge. We note that the apparent non-periodic pattern of the orbital evolution, especially noticeable in the case of the 0.36 $M_\odot$ companion, is because we can only store every 10th model when we run a long simulation. We have checked that if we store every model for a period of time, the apparent pattern disappears, and during the slow spiral-in, each binary has constant, albeit slowly decreasing, orbital period, as expected. The orbital energy does not oscillate, but due to the nonzero eccentricity, the orbital separation, measured at particular times, shows oscillations. The start of the displayed orbital evolution on the left-hand panel corresponds to the moment of time when the orbital decay is increasing to $|(\dot{a}\,P_{\rm orb})|/a = 0.03$ for the binary with 0.05 $M_\odot$ companion, $|(\dot{a}\,P_{\rm orb})|/a = 0.01$ for the binaries with 0.10, 0.15, and 0.20 $M_\odot$ companions, and $|(\dot{a}\,P_{\rm orb})|/a = 0.005$ for the binary with 0.36 $M_\odot$ companion. For each case, the start of the plunge-in, when $|(\dot{a}\,P_{\rm orb})|/a$ becomes greater than 0.1, is indicated with a star symbol. The end of the plunge-in, when $|(\dot{a}\,P_{\rm orb})|/a$ becomes less than 0.1, is indicated with a circle symbol. The start of the slow spiral-in, when $|(\dot{E}_{\rm orb}\,P_{\rm orb})/E_{\rm orb}|$ becomes less than 0.01, is indicated with a square symbol. A triangle symbols indicates when $|(\dot{E}_{\rm orb}\,P_{\rm orb})/E_{\rm orb}|$ becomes less than 10^{-4}.

been assigned to be 'mergers', while in Nature, if the companions are compact, CEEs in these binaries could result in a slow spiral-in with an orbit that is smaller than our cut-off distance 0.15 $R_\odot$.

In the following sections, we will discuss the differences in the processes that may lead to these three types of the outcomes. We will refer to the binary formation case with 0.36 $M_\odot$ companion as BF36, to the slow spiral-in cases with 0.20 and 0.15 $M_\odot$ companions as SS20 and SS15, and to the merger cases with 0.10 and 0.05 $M_\odot$ companions as M10 and M05.

3 MAPPING AND SYMMETRY

In this section, we introduce the mapping tools that convert the results of 3D simulations to 1D space, both for the analysis of physical processes that will be done in this paper, and for the possible future comparisons with 1D simulations of CEEs.

The outcomes of hydrodynamical simulations are not fully symmetrical, while a typical evolutionary stellar code deals with a spherically symmetric 1D star. In the 1D case, the centre of symmetry is naturally located at the centre of the modelled star, in its core. The centre of a 3D object during and after a CEE is not that indisputable. During the Phase I, only the outer layers are perturbed, and the donor star mainly keeps its original symmetry around the core. During the dynamical Phase II, no symmetry can be expected. Finally, during the Phase III, symmetry – from the dynamic point of view – is expected to form around the centre of mass of the binary that rotates inside the CE. However, this phase may continue long enough that the energy transport starts to affect the envelope's temperature and density profile (self-regulated spiral-in). On one hand, the energy transport will be symmetric around the nuclear energy source, if that nuclear energy source (e.g. shell burning) is still active. On the other hand, the binary's orbital energy release may stem from a different point and shift the average centre of symmetry, as the energy generation rate can outpace the nuclear energy source. It is inevitable therefore that no true spherical symmetry can exist, but we can evaluate how the choice of the centre of symmetry can affect the anticipated 1D spherically symmetric stellar structure.

The mapping of our 3D object to 1D object is done by using a mass-weighted average of a given quantity over a spherical shell of radius, r and thickness, δr:

$$\bar{X}(r) = \frac{\sum_k x_k m_k}{\sum_k m_k}. \quad (1)$$

Here $\bar{X}(r)$ is a discrete (mesh-type, similar to 1D stellar profiles) profile of the quantity X, the mesh-points spaced by δr. The variable x_k is the value of the quantity X that an SPH particle k has, m_k is the mass of the same SPH particle k, and k is the index of the SPH particle. The summation goes over all particles k such that the distance from each particle to the chosen centre, r_k, is between r and δr.

We compare the two choices for the centre of symmetry, the red giant core and the centre of mass of the binary during a

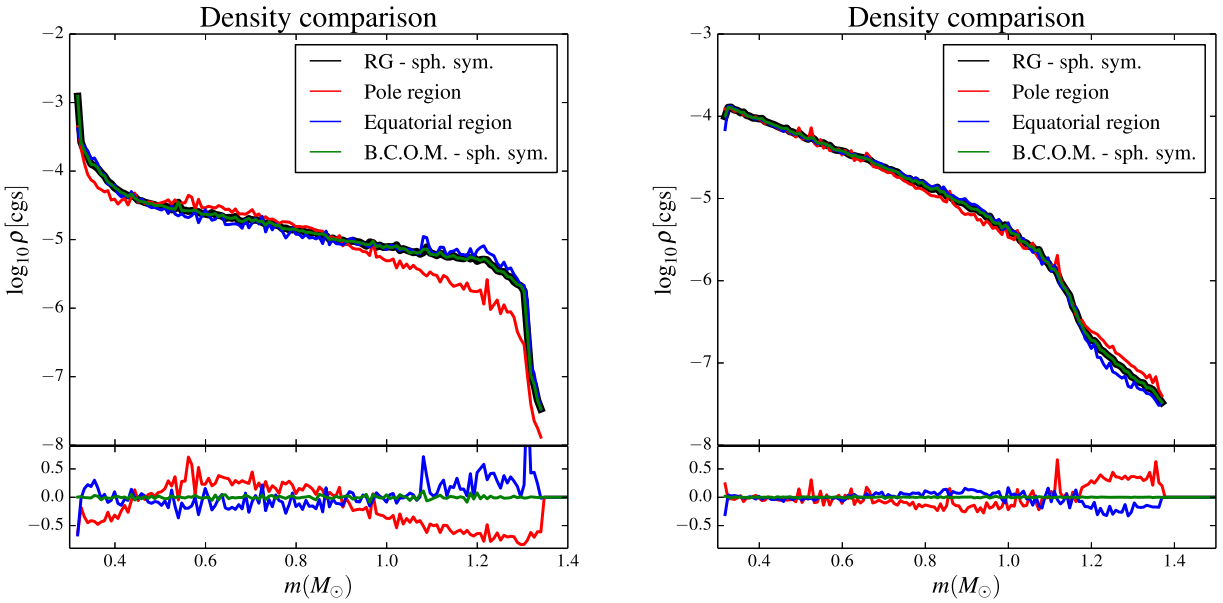

Figure 2. Comparison of the ways to average quantities, shown on the example of density. The left-hand panel shows the case BF36 just before the end of the plunge-in, when outflows are significant (day 364).The right-hand panel shows the case SS15 at the start of the slow spiral-in, where there is almost no outflows (day 645). Shown are four ways to average the quantity: with the red giant core at the centre and the entire CE object $\rho_{\rm RG}$ (thick black), same centre of symmetry and only the polar region $\rho_{\rm pole}$ (red), same centre of symmetry and only the equatorial region $\rho_{\rm equat}$ (blue), and finally with the centre at the centre of mass of the binary, averaged over the entire CE object $\rho_{\rm BCOM}$ (green). The bottom panels show the ratios of the three latter quantities to the first, $(\rho_{\rm pole}-\rho_{\rm RG})/\rho_{\rm RG}$ (red), $(\rho_{\rm equat}-\rho_{\rm RG})/\rho_{\rm RG}$ (blue), and $(\rho_{\rm BCOM}-\rho_{\rm RG})/\rho_{\rm RG}$ (green).

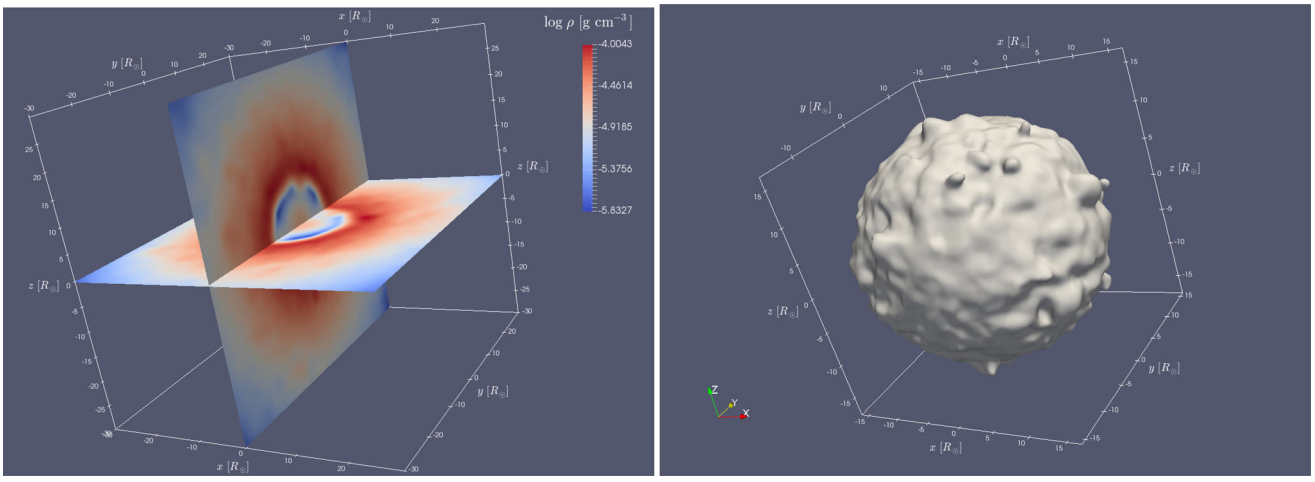

Figure 3. Density distribution during a slow spiral-in, the case SS15 (day 747). The left-hand panel shows density slices in the orbital plane and in the perpendicular plane. The right-hand panel shows a contour figure for $\log_{10}\rho=-4.3$. The orbital separation at this moment is $a=0.18\,{\rm R}_\odot$, the binary is not resolved. This is a zoom-in, not the entire CE object is shown. This figure shows the system 122 d after the start of the slow spiral-in. By this time, the formed close binary has orbited about 8000 times, and about $0.5\,{\rm M}_\odot$ of the envelope mass is ejected. Please note that the densiest part of the hollow shell, while symmetric overall, is still 'clumpy.' The figures were created using ParaView (Ahrens, Geveci & Law 2005; Ayachit 2015).

well-established spiral-in, i.e. the formed binary has made a few thousand orbits. We find that for the layers outside of the orbit, the choice of the centre of symmetry is less significant, and the differences between the averaged values are within a few per cent (see Fig 2). The large number of the periods is expected to result in a spin-up of most of the mass that is located within a few binary orbits around the centre of mass of the binary. Indeed, we note that independently on the centre's choice, there is almost no stellar material within a few orbits around the centre of mass of the binary. For example, consider the case of simulation SS15 at the moment when 122 d have passed after the start of the slow spiral-in, or about 8000 binary periods. The orbital separation at that time is $\sim$0.2 $\rm R_\odot$. Except for the only two SPH particles that are within the RL of the companion, and two more particles that are located at about 6 $\rm R_\odot$, all the other SPH particles are located at least beyond 8 $\rm R_\odot$ from the binary, creating a pronounced density inversion around the binary for about 40 orbital separations (see Fig. 3).

We note that the density inversion was observed in previous 3D CEE simulations, for example, see the study by Passy et al. (2012). In their work, the CEE simulations were done with the two types

of the numerical methods and compared with an SPH type code and with a grid-based code. We note that there the density inversion was more pronounced in simulations with an SPH code, than with a grid based code, and we attribute it to the reason we described above. We should, however, stress that in our case, we discuss the state of the CE system when the formed close binary has revolved for about 8000 orbital periods, affecting its neighbourhood, while in Passy et al. (2012), the density profiles are made for a moment when the formed binary has made less than 50 orbital periods. Using our definitions of the CEE phases as in Section 2, their binary has just started the slow spiral-in and has had less 'relative' time to spin-up its neighbouring SPH particles. At the similar stage of the CEE – the start of the spiral-in – our envelope had not yet formed a hollow shell.

We note as well that in 1D CEE simulations, such a strong density inversion and core stripping have never been reproduced (see, e.g. fig. 2.8 in Ivanova 2002, where also a low-mass giant case was considered). This is likely relevant to the fact that 1D stellar codes, when modelling a CEE, add the energy as a 'heat' instead of the mechanical energy (we will discuss how the form of the added energy affects the outcomes in Sections 6 and 7). Another plausible reason is that the tidal spin-up of the envelope from the binary is not taken into account as it should be, and the spin-up is deposited at an incorrect location.

We anticipate that the decoupling between the binary and the envelope might be partially a numerical problem, due to the small number of particles that are left near the binary, and the smoothing length in that region. Unfortunately, decreasing the mass of SPH particles by a factor of two, increasing thereby a simulations' resolution by a factor of 2, we run in the same problem when decreasing the smoothing length to obtain a better value for the gravitational potential, as was discussed in Section 2. None the less, we believe that the formation of a hollow shell is a physical phenomenon by virtue of a tidal spin-up that operated during many binary time-scales.

We can also compare profiles of thermodynamic quantities for 'polar' SPH particles (those particles that have a polar angle within $\vartheta < 25^0$ around the zenith direction that goes through the red giant core, and for negative Z, $\vartheta > 155^0$), and for 'equatorial' SPH particles (those that are located close to the equatorial plane and have their polar angle within $75^0 < \vartheta < 105^0$). To be more specific, the mass–radius relation for the coordinates is the same as for the averaging of the whole 3D object, but the average values of any quantity are found only for the particles that are within these polar angles.

We find that, as expected, at the end of the plunge-in, the asymmetry is strong – up to an order of magnitude difference in values that can be found in polar and equatorial directions (see Fig. 2, the left-hand panel). The most pronounced deviations are for the polar direction, where density and pressure are substantially lower than their averages over all angles in the proximity of the binary orbit and at large radii, while denser in between. This is likely because of the active ongoing 'outflows' in the equatorial direction, which are compensated by somewhat slower 'inflows' in the polar direction.

During a slow spiral-in, when the binary orbit almost does not decay during several dynamical time-scales of the expanded envelope (e.g. 40 d in case SS15), non-negligible asymmetry is still present. Qualitatively, the density profiles in opposite directions are consistent with deviations expected from rotation. Relative differences for the density in polar and equatorial directions in the extended envelope, still can reach a factor of a few, with the density in the equatorial direction being smaller (when taken at the same distance from the red giant core).

4 ENERGIES

4.1 Energies definitions in a 1D approach

In the 1D approach, the gravitational potential, or the specific gravitational potential energy in the envelope during a CEE is

$$\phi_{\rm env1D}(r) = -\left(\frac{Gm(r)}{r} + f_{\rm ins}\frac{GM_{\rm comp}}{r}\right) . \quad (2)$$

Here $m(r)$ is the local mass coordinate within the star (excluding the companion), r is the radial coordinate, $f_{\rm ins}$ indicates the effect of the companion, and $f_{\rm ins} = 1$ if the companion orbits within r, or $f_{\rm ins} = 0$ if the companion orbits outside r. The origin of the second term in this equation will be explained in more detail in Section 4.3.

The potential energy of the envelope $E_{\rm pot,env1D}$ (the envelope is everything except what is defined as the core, which can be ambiguous; see Ivanova 2011), the internal energy of the envelope $E_{\rm int,env1D}$ (this energy consists of the thermal energy of the envelope $E_{\rm th,env1D}$ and the recombination energy of the envelope $E_{\rm rec,env1D}$), the binding energy of the envelope, and the kinetic energy of the envelope $E_{\rm kin,env1D}$, are defined as (see also Ivanova et al. 2013a)

$$E_{\rm pot,env1D} = -\int_{M_{\rm core}}^{M}\left(\frac{Gm}{r} + f_{\rm ins}\frac{GM_{\rm comp}}{r}\right) {\rm d}m \; ; \quad (3)$$

$$E_{\rm th,env1D} = \int_{M_{\rm core}}^{M} e_{\rm th}\, {\rm d}m \; ; \quad (4)$$

$$E_{\rm rec,env1D} = \int_{M_{\rm core}}^{M} \varepsilon_{\rm rec}\, {\rm d}m ; \quad (5)$$

$$U_{\rm int,env1D} = \int_{M_{\rm core}}^{M} u\, {\rm d}m = E_{\rm th,env1D} + E_{\rm rec,env1D} \; ; \quad (6)$$

$$E_{\rm bind,env1D} = U_{\rm int,env1D} + E_{\rm pot,env1D} \; ; \quad (7)$$

$$E_{\rm kin,env1D} = \int_{M_{\rm core}}^{M} 0.5V^2\, {\rm d}m . \quad (8)$$

Here M is the total mass of the star, m is the local mass coordinate, u is the specific internal energy and $u = e_{\rm th} + \varepsilon_{\rm rec}$, $\varepsilon_{\rm rec}$ is the specific recombination energy, and $e_{\rm th}$ is the specific thermal energy for which no recombination energy is taken into account. V is velocity; note that in 1D, velocities for $E_{\rm kin,env1D}(M_{\rm core})$ do not include the donor's movement on its binary orbit, but only the relative velocities in the corotation frame. The recombination energy $E_{\rm rec,env1D}$ is static potential energy, which is not available immediately and is only released as a response of the envelope on its expansion. This energy release may or may not be triggered during a CEE (Ivanova, Justham & Podsiadlowski 2015).

4.2 Energies definitions in a 3D SPH code

In a 3D approach, the gravitational potential that a particle i has is defined as

$$\phi_i = \sum_{l\neq i}^{N} m_l \varphi_{i,l} \, , \quad (9)$$

where $\varphi_{i,l}$ is the gravitational potential between two SPH particles of unit mass that have a distance between them $|\boldsymbol{r}_i - \boldsymbol{r}_l|$ (technical

details on how it is calculated can be found in Hernquist & Katz 1989).

The potential, internal, recombination, and kinetic energies of an SPH particle are

$$E_{\rm pot,}_k = m_k \phi_k, \tag{10}$$

$$U_{{\rm int},k} = m_k u_k, \tag{11}$$

$$E_{{\rm rec},k} = m_k \varepsilon_{\rm rec}, \tag{12}$$

$$E_{{\rm kin},k} = 0.5 m_k \left(v_{x,k}^2 + v_{y,k}^2 + v_{z,k}^2\right) . \tag{13}$$

Here $v_{x,k}$, $v_{y,k}$, and $v_{z,k}$ are integrated from the equations of motion (i.e. they are calculated with respect to the coordinate system). The variable u_k in our SPH code is integrated over time using the equation of thermal energy change (as in Monaghan 2002; Gaburov et al. 2010), an implementation that guarantees conservation of total energy and entropy in the absence of shocks. $\varepsilon_{\rm rec}$ is a component of u_k. The total energy of a CE system that consists of the envelope (the gas that is not yet ejected to infinity), the donor's core and the companion, is

$$\begin{aligned} E_{\rm tot,CE} &= \sum_k^N (0.5 E_{{\rm pot},k} + U_{{\rm int},k} + E_{{\rm kin},k}) \\ &= \sum_k^N 0.5 m_k \sum_{l \neq k}^N m_l \varphi_{k,l} + U_{\rm int,CE} + E_{\rm kin,CE} . \end{aligned} \tag{14}$$

Here the summations goes over all SPH particles that are still gravitationally bound to the CE system. The total internal energy of the CE system is the same as the energy of the envelope, $U_{\rm int,CE} = U_{\rm int,env3D}$.

The first term in the equation (14) is the total potential energy of the CE system:

$$E_{\rm pot,CE} = \sum_k^N 0.5 m_k \sum_{l \neq k}^N m_l \varphi_{k,l} . \tag{15}$$

The potential energy of the envelope consists of such components as the potential energy between the envelope and the core $E_{\rm pot,e\text{-}core}$, the self-gravitating energy of the envelope $E_{\rm pot,e\text{-}sg}$, and the potential energy between the envelope and the companion $E_{\rm pot,e\text{-}comp}$:

$$\begin{aligned} E_{\rm pot,env3D} = \sum_k^{\rm Env} m_k \Bigg(& M_{\rm core} \varphi_{k,{\rm core}} + 0.5 \sum_{l \neq k}^{\rm Env} m_l \varphi_{k,l} \\ & + M_{\rm comp} \varphi_{k,{\rm comp}} \Bigg) , \end{aligned} \tag{16}$$

where the summation is only for the normal (non-special) particles belonging to the envelope. The potential energy of the CE system is then

$$E_{\rm pot,CE} = E_{\rm pot,env3D} + M_{\rm comp} M_{\rm core} \varphi_{\rm comp,core},$$

and the total energy of the CE system is

$$\begin{aligned} E_{\rm tot,CE} = {} & U_{\rm int,env3D} + E_{\rm pot,env3D} \\ & + E_{\rm kin,CE} + M_{\rm comp} M_{\rm core} \varphi_{\rm comp,core}. \end{aligned} \tag{17}$$

The 'orbital energy' of the binary system is (see, e.g. Nandez et al. 2015):

$$\begin{aligned} E_{\rm orb,3D} = {} & 0.5 \mu |V_{12}|^2 + 0.5 \sum_i^{\rm RL1,RL2} m_i \phi_i \\ & - 0.5 \sum_j^{\rm RL1} m_j \phi_j^{\rm RL1} - 0.5 \sum_k^{\rm RL_2} m_k \phi_k^{\rm RL_2} , \end{aligned} \tag{18}$$

where $\mu = M_1 M_2/(M_1 + M_2)$ is the reduced mass, and $\boldsymbol{V}_{12} = \boldsymbol{V}_1 - \boldsymbol{V}_2$ is the relative velocity of the two stars. The first term gives the kinetic energy. The second term is the gravitational energy of the binary, with the sum being over all particles i that are inside the two immediate RLs, where each RL depends on the mass of all particles that are bound to the whole mass within that RL, and are not simply functions of the masses of the RG core and the companion. The third and the fourth terms correspond to the removal of the self-gravitational energy of the donor (the sum being over particles j within the RL of the star 1) and of the companion (the sum being over particles k within the RL of the star 2), respectively. The caveat here of course is that during a plunge-in, there is no orbit, and the orbital energy found using equation (18) is not related to the separation between the particles.

It can be seen that the orbital energy $E_{\rm orb,3D}$ and the potential energy of the envelope $E_{\rm pot,env3D}$ have some similar terms – the potential energy between the particles in the RL of the companion and the core, the potential energy between the particles in the RL of the core and the companion, and the potential energy between the particles in the two different RLs. That is because a particle, when it is inside the RL, is both part of the envelope and of the binary. Therefore, it is not possible to decompose the total potential energy of the CE system into the intrinsic potential energy of the binary and the potential energy of the envelope.

Instead, we can introduce the *reduced* orbital energy, where only the core and the companion are considered:

$$\begin{aligned} E_{\rm orb,CC} = {} & 0.5 M_{\rm core} v_{\rm core}^2 + 0.5 M_{\rm comp} v_{\rm comp}^2 \\ & + M_{\rm comp} M_{\rm core} \varphi_{\rm comp,core} . \end{aligned} \tag{19}$$

Note that this energy cannot, in principle, determine the current orbital separation of the binary. We stress that to find the orbital separation a after the plunge using energy, one has to use $E_{\rm orb,3D}$; during the plunge, there is no orbital separation–energy relation.

We also introduce the kinetic energy of the envelope

$$\begin{aligned} E_{\rm kin,env3D} = {} & 0.5 \sum_k^{\rm Env} m_k v_k^2 \\ = {} & E_{\rm kin,CE} - 0.5 M_{\rm core} v_{\rm core}^2 - 0.5 M_{\rm comp} v_{\rm comp}^2 . \end{aligned} \tag{20}$$

Unlike the 1D case, this energy is non-zero even at the beginning, since the star's envelope rotates with the binary.

Finally, we can rewrite the energy equation of the CE system as

$$E_{\rm tot,CE} = E_{\rm orb,CC} + U_{\rm int,env3D} + E_{\rm pot,env3D} + E_{\rm kin,env3D} . \tag{21}$$

Note that in a 3D code, the total energy of all particles (including those that are unbound) is conserved but this is not so for $E_{\rm tot,CE}$. Hence, this equation can serve as the energy conservation only if no particles have become ejecta.

4.3 The energy conservation in 1D

Let us transfer the energy conservation equation (21) to 1D. As previously, this is for the case when there is no ejecta.

1. *The internal energy:*

$$U_{\rm int,env3D} = U_{\rm int,env1D}\,. \tag{22}$$

2. *The orbital energy* can be described using binary orbital energy:

$$E_{\rm orb,CC} = -\frac{GM_{\rm core}M_{\rm comp}}{2a}\,. \tag{23}$$

Note that this is *not* valid during a plunge, where instead equation (19) should be used.

3. *The kinetic energy:* there is no simple direct link between $E_{\rm kin,env3D}$ and $E_{\rm kin,env1D}$. In the first case, one measures velocities in a stationary reference frame that moves with the centre of mass, and in the second case, velocities are measured in the corotation frame. Before the plunge, $E_{\rm kin,env3D} \simeq GM_{\rm env}M^2_{\rm comp}/(2a(M+M_{\rm comp}))$, and after the plunge, if the angular velocities in the spun-up envelope are taken into account for 1D, $E_{\rm kin,env3D} \simeq E_{\rm kin,env1D}$.

4. *The potential energy:* in 1D, an added mass inside the envelope (an orbiting companion) technically produces the same potential as a 'thin spherical shell.' A 'thin spherical shell' does not create a potential inside of it, nor does it create a gravitational force that would act on an object inside of it (Newton's shell theorem). This is why the potential energy in 1D is written as in equation (3) (in Section 4.4, we also will discuss what error is produced by the thin shell approximation in equation (3), i.e. for the CE that is outside of the companion's orbit). The difference between 3D and 1D potential energy should include $E^{\rm out}_{\rm pot,e\text{-}comp}$, which is the fraction of $E_{\rm pot,e\text{-}comp}$ that sums only over the SPH particles that are inside the companion's orbit. Note that if thin shell approximation is taken to be valid at any moment of the CEE evolution, it will also imply that $E^{\rm out}_{\rm pot,e\text{-}comp} = 0$ when the companion is still outside of the envelope. However, at the same moment, the true value is well approximated by the point mass expression, $E^{\rm out}_{\rm pot,e\text{-}comp} \simeq -GM_{\rm env}M_{\rm comp}/a$. As a result, in 1D, a partially inconsistent approach is usually taken: for the envelope mass outside of the orbit, the companion is treated as a thin shell (this is the second term in equation (3)); and for the envelope mass inside of the orbit, $m_{\rm env}(r<a)$, the companion is treated as a point mass, $E^{\rm out}_{\rm pot,e\text{-}comp} = -Gm_{\rm env}(r<a)M_{\rm comp}/a$.

We can now rewrite the energy conservation equation (21) using '1D values':

$$\begin{aligned} E_{\rm tot,CE} = 0.5\left(M_{\rm core}v^2_{\rm core} + M_{\rm comp}v^2_{\rm comp} + \int_{M_{\rm core}}^{M} v^2{\rm d}m\right) \\ + \int_{M_{\rm core}}^{M}\left(u - \frac{Gm}{r}\right){\rm d}m - \frac{GM_{\rm core}M_{\rm comp}}{a} \\ - \int_{m(r>a)}^{M}\frac{GM_{\rm comp}}{r}{\rm d}m - \frac{Gm_{\rm env}(r<a)M_{\rm comp}}{a}\,, \end{aligned} \tag{24}$$

where all velocities are in the inertial frame, and velocities of the core and the companion are not related in a simple way to the orbital separation, especially during the plunge.

After the plunge-in, a simplification can be made:

$$\begin{aligned} E_{\rm tot,CE} = -\frac{GM_{\rm core}M_{\rm comp}}{2a} + 0.5\int_{M_{\rm core}}^{M} v^2{\rm d}m \\ + \int_{M_{\rm core}}^{M}\left(u - \frac{Gm}{r}\right){\rm d}m \\ - \int_{M_{\rm core}}^{M}\frac{GM_{\rm comp}}{r}{\rm d}m\,. \end{aligned} \tag{25}$$

In conclusion, given the complications with the kinetic energy, the potential energy, and the non-Keplerian orbit of the companion during the plunge, a 1D code cannot self-consistently conserve energy during the plunge-in.

4.4 The validity of the thin shell approximation

To assess the thin shell approximation for the fraction of the envelope that is outside of the orbit, we can find the 'reduced' 3D gravitational potential for each SPH particle in the envelope, $\phi_i^{\rm red}$, in a way that will measure the same quantity as does the 1D definition for the gravitational potential:

$$\phi_i^{\rm red}(r) = \sum_{l\neq i}^{\leq r} m_l\varphi_{i,l} + M_{\rm core}\varphi_{i,\rm core} + f_{\rm ins}M_{\rm comp}\varphi_{i,\rm comp}\,, \tag{26}$$

where the summation is only for envelope particles that have a distance to the chosen 'centre' smaller than r. As previously, for the numerical mapping from 3D to 1D, $\phi^{\rm red}_{\rm 3D}(r)$ is found by averaging the particles that have r within some small neighbourhood $[r; r+\delta r]$. Summed over all the envelope particles, this quantity produces the equivalent of $E_{\rm pot,env1D}$.

As can be expected, at the end of the plunge-in, the difference between the 3D averaged value for $\phi^{\rm red}_{\rm 3D}$ and the 1D value $\phi^{\rm red}_{\rm env1D}$ is small (see Fig. 4). However, during the plunge-in, the 1D approximation often provides a significantly less negative potential well in the envelope near the companion than the 3D model provides for $\phi^{\rm red}_{\rm 3D}$. The deviation can be as large as 50 per cent of the value over a region of several solar radii. After the envelope had decoupled, the gravitational potential within the inner envelope's 'shell' is also not in good agreement between the two approaches.

By its design, this comparison only demonstrates the effect of the companion on the difference between the two potentials above the orbit. However, the full potential inside the orbit will also depend on the companion. Typically, the 3D approach provides a deeper potential well in the neighbourhood of the orbit, while far above the orbit, the potential well can be more shallow than in the 1D thin shell approximation (see Fig. 4). The value of the specific potential energy does not affect the structure calculations in a 1D model, which are affected only by the value of the local gravitational acceleration. Note that this is a post-processed value. However, it plays a role in what is considered in 1D simulations as the immediate energy budget as well as the rate of the energy transfer from the orbit to the envelope, and therefore may affect the rate of the orbital dissipation.

4.5 Where and in what form the orbital energy is deposited

In both 3D and 1D approaches, the recombination energy is deposited self-consistently where it has been released. This is not the same for the orbital energy release. A 1D approach must come up with a prescription on how to deposit the energy that corresponds to the independently obtained orbital dissipation. We can get a hint from our 3D simulations on where the orbital energy is effectively deposited, and in what form it is deposited.

In Fig. 5, we show where the local specific energies are changing while the orbit is shrinking. It can be seen that the potential energy and the kinetic energy are clearly increasing everywhere above the orbit, while the internal energy is changing at a much smaller pace than that of the potential and kinetic energies. As expected, the change in the real potential above the orbit is similar to that of the reduced potential. In the regions where the orbit had passed between the two moments of time for which the derivatives are found, the

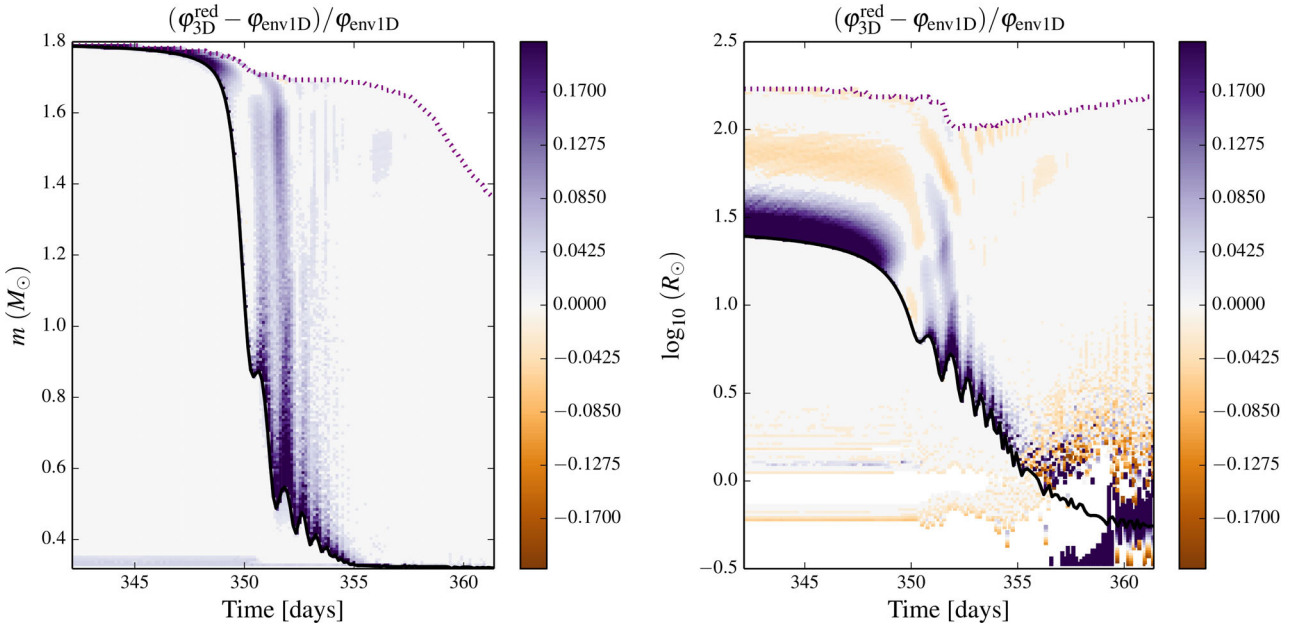

Figure 4. Comparison of the gravitational potentials in 1D and 3D approach, shown for the example of BF036. The left-hand panel shows the difference as a function of mass, and the right-hand panel shows the same difference but as a function of radius. The solid black lines indicate the location of the companion. To help to distinguish colour shades, we indicate with the dashed purple lines the surface of the envelope. As we only show the bound mass, the surface is defined as either the mass coordinate of a bound particle that is farthest away from the centre of the symmetry (for the left-hand plot), or the farthest distance from the centre of the symmetry for bound particles (for the right-hand plot). The surface in the plots should not be confused with the stellar photosphere, which is not obtained in our simulations.

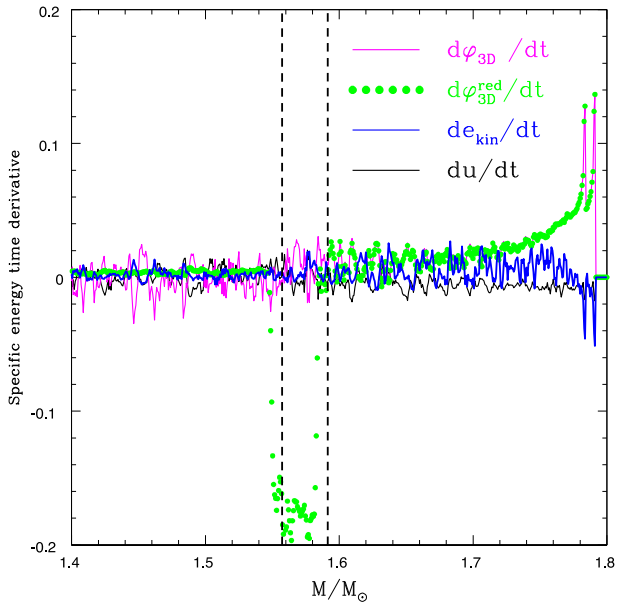

Figure 5. Energy changes in case SS15, day 615. Time derivative of the specific energies are in units of 10^{15} erg s^{-1}. e_{th} here includes both thermal and recombination energies. Derivatives are calculated between the two snapshots of 3D simulation. The locations of the companion's orbits for the two time moments are shown with vertical dashed black lines.

absolute value of the time derivative of the reduced potential is a couple of orders of magnitude larger than that of the real potential. Below the orbit, the 3D potential derivative is substantially more noisy than that of the reduced potential, as it is affected by the entire envelope above. The derivatives indicate that we cannot detect the orbital energy deposition inside the binary orbit, but outside of the orbit it affects the entire envelope, primarily changing the mechanical energy of the envelope – the potential energy and the kinetic energy (and kinetic energy is converted to the potential energy with time). This will become important in Section 7, where we will discuss how the form of the energy deposition may affect the outcome.

5 ANGULAR MOMENTUM

5.1 Average angular momentum in 3D case

The Z-component of the angular momentum for each SPH particle is found with respect to a particular point that should be moving without acceleration (for technical details, see Appendix A; below, whenever we talk about an angular momentum, we will imply only its Z-component). However, the core of the red giant – our preferred centre of symmetry for other CE system properties – is not stationary, nor is it moving at a nearly constant velocity. On the contrary, the core is orbiting around a point which, at least during the slow spiral-in, coincides well with the centre of mass of the core-companion binary system. The angular momentum therefore cannot be calculated with respect to the core, and if such a calculation is carried out, the value of the angular momentum oscillates.

We choose therefore to calculate the averaged angular momentum with respect to the centre of the core-companion binary. The caveat with this approach is that the centre of mass of the binary can also be moving with an acceleration. Therefore, during the plunge-in phase, this averaged quantity is also not entirely meaningful, and becomes most useful only at the end of the spiral-in. In Fig. 6, we show the accumulated gain in the specific angular momentum in the envelope, computed from the start of the CEE simulation.

There are two important features that are present in all the simulations.

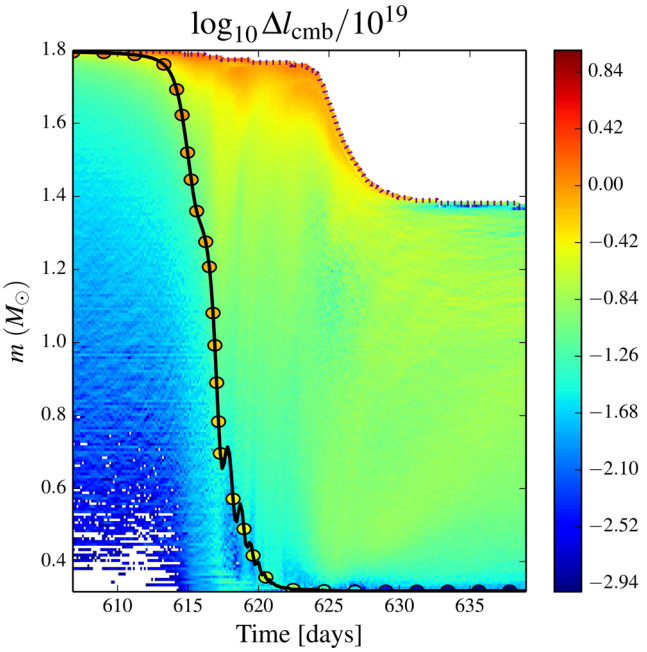

Figure 6. Accumulated gain in the average specific angular momentum, shown for the case SS15. The black solid line shows the instantaneous orbital separation between the core and the companion. The colours of the circles indicate the Keplerian specific angular momentum that this location would have. The dashed purple line indicates the surface of the envelope. White colour implies that the accumulated gain at this location is below the cut-off minimum value, $\log_{10}\Delta l_{\rm cmb} < -3$.

(i) We do not see that the region inside the orbit gains angular momentum or spins up. While we have said that the value of the average angular momentum is not fully self-consistent before the slow spiral-in, the almost complete absence of any spin-up is none the less important.

(ii) Most of the initial binary angular momentum is absorbed by the outer layers of the envelope. It is those layers that get ejected during the plunge-in, leaving the remaining CE with a smaller fraction of the total initial angular momentum (this can be seen both in Fig. 6 and from data shown in Table 1).

5.2 Angular velocity for 1D star

To understand how to relate our 3D star to a 1D star, we will briefly review how the treatment of rotation is done for 1D stars in stellar codes. Generally, angular momentum transport is calculated using a diffusion equation. A diffusion equation is meant to trace and to be written implicitly for the angular momentum, while in practice, it is usually written using the angular velocity variable. Currently, there are several ways to write the diffusion equation, however, the basis for all of them is (Endal & Sofia 1978)

$$\frac{\partial\Omega}{\partial t} = \frac{1}{\rho r^4}\frac{\partial}{\partial r}\left(\rho r^4 D\frac{\partial\Omega}{\partial r}\right). \quad (27)$$

Here D is some diffusion coefficient, and Ω is angular velocity. The differences between several modern modifications are then based on what kinds of instabilities are taken into account to find the diffusion coefficient D. A more complete form of the diffusion equation can also take into account the flux due to non-zero radial velocity, and the temporal loss of the angular momentum (e.g. see for technical details appendix in Ivanova 2002).

It is important that the transition from the angular momentum as a 'diffusing quantity' to the angular velocity as the main variable can be done only by choosing and fixing the relation between angular velocity and specific angular momentum. Specifically, the above diffusion equation (27) adopts the assumption that the angular velocity is only a function of radius. This allows a simplification in which the star is treated as if it is composed of thin spherical shells, where each shell has constant angular velocity, and has specific moment of inertia $i = 2/3r^2$.

At the same time, it is anticipated that the centrifugal force affects the local effective gravity. Hence, mass shells need to correspond to isobars rather than to spherical shells (for methods, see e.g. Endal & Sofia 1976; Heger & Langer 1998; Heger, Langer & Woosley 2000; Paxton et al. 2013). As a result, in stellar codes where isobars are considered, stellar structure variables are taken as being constant on isobars, while the angular momentum diffusion is still based on spherical symmetry.

In this paper, we chose to reduce the 3D angular momentum distribution into a 1D angular velocity distribution by adopting the same relation between the specific angular momentum and the angular velocity as was done implicitly for the angular momentum diffusion equation (27). Therefore, we provide values of $\Omega(r)$ as averaged on spherical shells.

There are two ways to do the averaging for the angular velocity. First, we can find the total angular momentum in a thin shell that is located at the radius r and has a thickness δr, and then use the relation for a specific moment of inertia of a thin shell:

$$\bar{\Omega}_{\rm spher}(r_{\rm shell})) = \frac{3}{2}\frac{\bar{l}(r)}{\bar{r}^2} = \frac{3}{2}\frac{1}{\bar{r}^2}\frac{\sum_{i\in{\rm shell}} l_i m_i}{\sum_{i\in{\rm shell}} m_i}. \quad (28)$$

Here the summation is only done for the particles which belong to the thin shell located at r with a thickness δr. On the other hand, we can also find the mass-averaged angular velocity at each shell:

$$\bar{\Omega}_{\rm mass}(r_{\rm shell}) = \frac{\sum_{i\in{\rm shell}} \Omega_i m_i}{\sum_{i\in{\rm shell}} m_i} = \frac{\sum_{i\in{\rm shell}} l_i m_i / r_{z,i}^2}{\sum_{i\in{\rm shell}} m_i}. \quad (29)$$

Here $r_{z,i}$ is the distance from the particle to the rotation axis.

We did not find a substantial difference between $\bar{\Omega}_{\rm mass}(r)$ and $\bar{\Omega}_{\rm spher}(r)$. There is some discrepancy for small values of the angular velocity, where more numerical noise is present in $\bar{\Omega}_{\rm spher}(r)$.

Like the case with the specific angular momentum, we do not observe a spin-up of the regions inside the orbit, and the Keplerian (binary) angular velocity always exceeds greatly that of the surrounding matter. There is only a short period of time when the matter around the orbit approaches close to the value of the binary angular velocity. This moment takes place just before the envelope material expands beyond the binary. It is close to the same time when the envelope and the inner binary have effectively decoupled, and the hollow shell structure seen in Fig. 3 started to form.

5.3 Angular velocity distribution during the slow spiral-in

At the start of the slow spiral-in, the specific angular momentum, unlike the case of a typical rotating star, does not rise monotonically from the centre to the surface. We can separate the envelope in two regions: the inner region, with an almost constant value of specific angular momentum, and the outer region, where the angular momentum was quickly transferred from the companion to the envelope during the plunge-in (see Figs 7 and 8). Between the two regions, the value of the specific angular momentum at the start of the spiral-in drops (see Fig. 7).

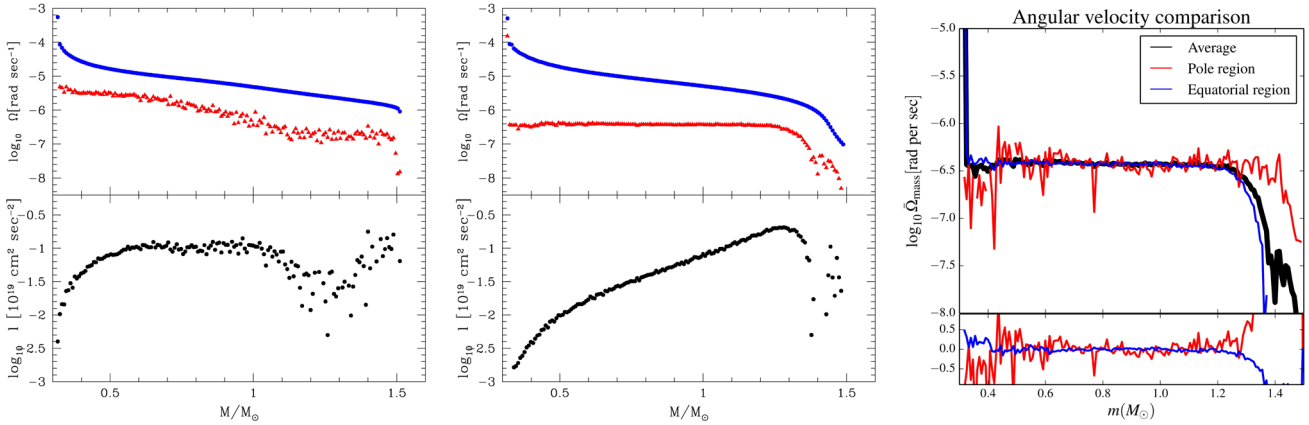

Figure 7. The mass-averaged angular velocity $\bar{\Omega}_{\rm mass}$ (red dots, top panels) and the specific angular momentum l (black dots, bottom panel), for the case M10. The blue dots on the top left and middle panels demonstrate the value of the Keplerian velocity that this envelope could have. The left-hand panel shows that case at the end of the plunge-in ($t = 613$ d), the middle panel shows the profiles 50 d later ($t = 664$ d, this is after the merger took place), and the right-top panel shows the comparison of the polar and equatorial regions for the same moment ($t = 664$ d). The bottom-right panel shows the ratio of the polar or equatorial angular velocities to the average.

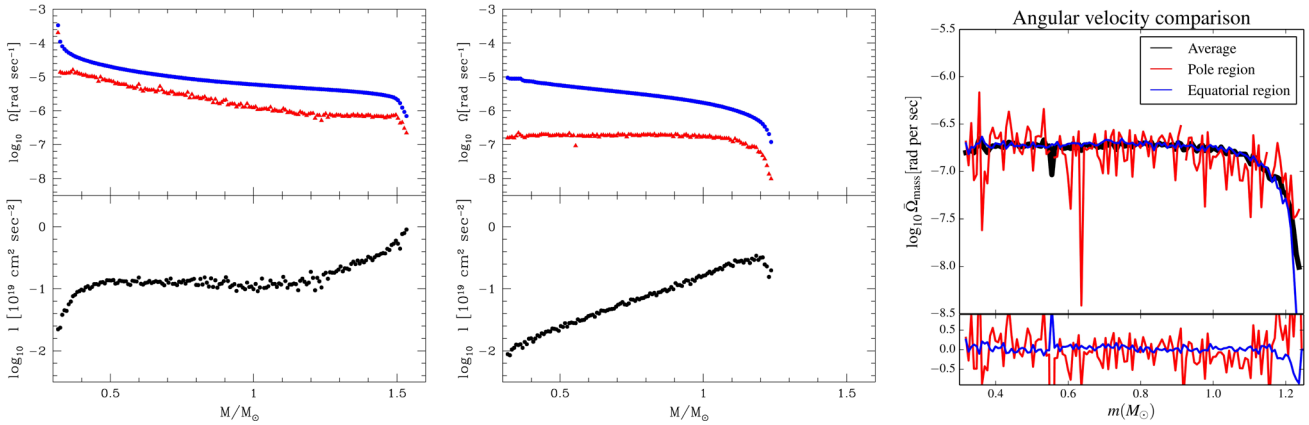

Figure 8. The mass-averaged angular velocity $\bar{\Omega}_{\rm mass}$ (red dots, top panels) and the specific angular momentum l (black dots, bottom panel), for the case SS15. The left-hand panel shows that case at the end of the plunge-in ($t = 626$ d), the middle panel shows the profiles 175 d later ($t = 801$ d), and the right-top panel shows the comparison of the polar and equatorial regions for the same moment ($t = 801$ d). Other information as in Fig. 7.

The angular velocity profile and the specific angular momentum profile evolve very quickly to 'stable' profiles after the plunge-in ends. In a stable situation, the specific angular momentum increases with the distance from the centre. This is established after about a few dynamical time-scales of the expanded CE, where $\tau_{\rm d,CE} \approx 50$ d. The angular velocity profile become flat in most of the envelope (by mass). The outer part of the envelope is small by mass but is more than 80 per cent of the envelope radius. There, the angular momentum transport is not efficient, and the angular velocity drops.

We note that either at the start of the slow spiral-in, or during the slow spiral-in, the angular velocity in the envelope is about an order of magnitude less than its local Keplerian velocity (see Figs 7 and 8). In none of our 3D simulations does the angular velocity of the inner part of the envelope approach the binary's angular velocity.

6 ENTROPY

In 1D studies, a common feature in the results is the formation of an 'entropy bubble' in the envelope (as can be seen in figures in e.g. Ivanova 2002; Ivanova et al. 2015). An entropy bubble is when part of the material of the envelope acquires a significantly higher entropy than it had before the CEE (note also, in convective envelopes, the pre-CEE entropy profile of a low-mass giant envelope is close to flat, with the exception of the surface layer). The entropy can increase by a factor of a few compared to its initial value. This high-entropy region also is often separated from the surface by a region where the entropy did not change strongly from its initial value, forming therefore an internal entropy bubble.

The reason for this entropy bubble formation is the way that the energy conservation is implemented in 1D codes. To conform with energy conservation, the energy that is released from the shrinking orbit has to be added to the envelope. And the commonplace way to do that is by adding a new 'luminosity' term in the energy equation (see e.g. Taam et al. 1978; Meyer & Meyer-Hofmeister 1979). This consideration, while using the term 'luminosity', is equivalent to adding the net heat dQ to the internal energy of the envelope material, and as a result, increases the entropy.

Recently, it has been shown that *where* the energy is added, does matter, and can define the outcome. The same overall energy input to the envelope, but added at different locations, can result either in

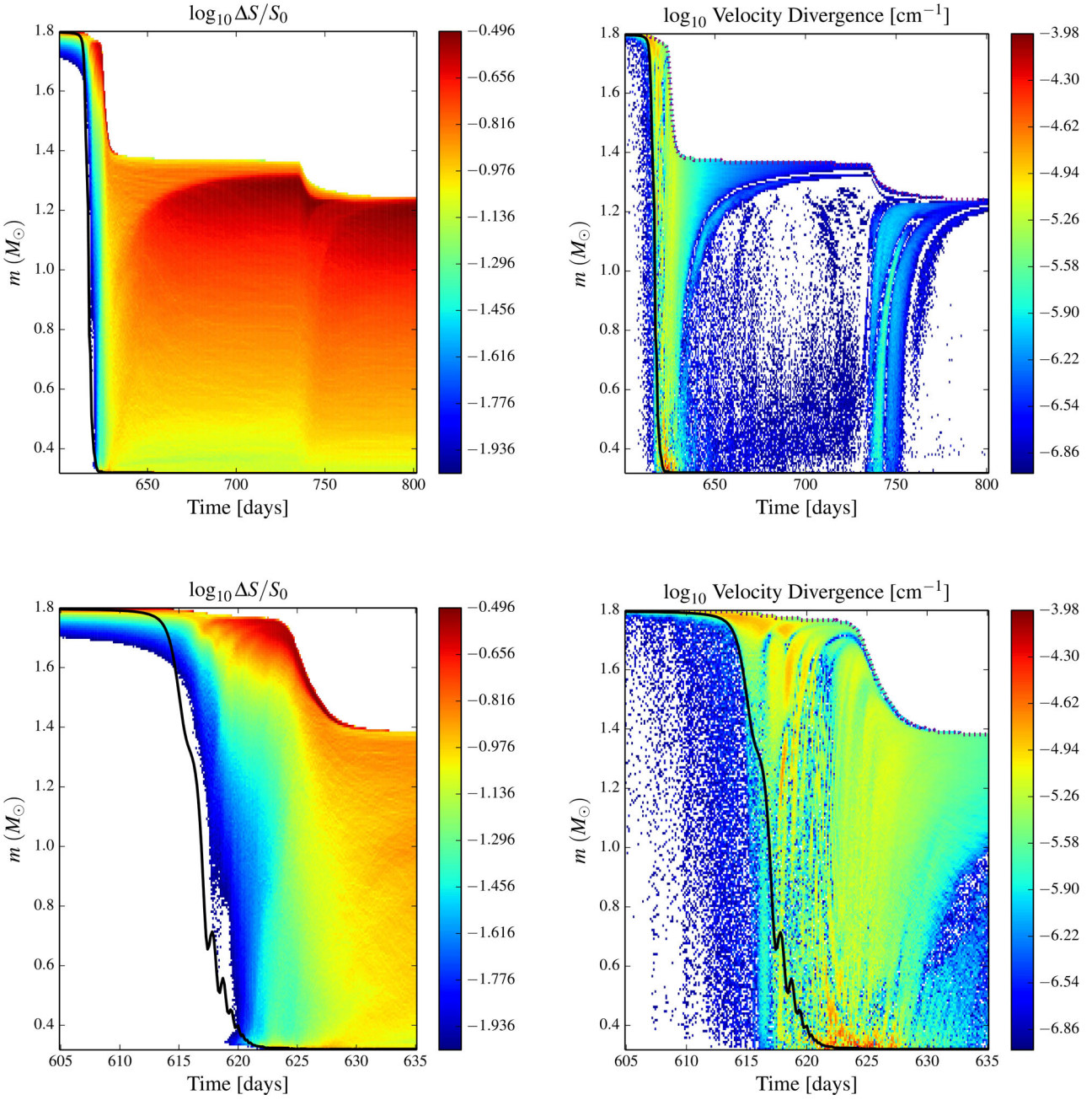

Figure 9. Entropy generation (shown as the ratio of the cumulative increase of the entropy from the start of the simulation, over its initial value, left-hand panels) and velocity divergence (right-hand panels). We show the case SS15. The top panels show long-term evolution, and the bottom panels show a zoom-in of the plunge-in phase. Black solid lines show the location of the companion. Dotted purple lines on the plots for velocity divergence indicate the surface of the envelope.

a slow spiral-in, or in the envelope's ejection (Ivanova et al. 2015). In Section 7, we will show that it matters in *what form* the energy is added, and the entropy is the key to understanding the difference.

In our 3D simulations, entropy is generated due to shocks and shear friction, where artificial viscosity leads to dissipation of local velocity differences by converting them into heat. As a sanity check, we have checked that our code provides perfectly adiabatic evolution when material recombines, if no shocks or other matter interactions between the particles are involved, and there is no artificial heating term. The velocity divergence is a good indicator of both shocks and a strong shear (see, e.g. discussion in Cullen & Dehnen 2010). Therefore, one of the best ways to trace the entropy generation is by looking at the velocity divergence (see Figs 9 and 10). The velocity divergence is one of the main variables in the SPH code we use and is calculated using equation 19 from Lombardi et al. (2006). We can distinguish how the entropy is generated during the three phases.

During phase I, prior to the plunge-in, when the companion's orbit is still outside the radius of the donor, we find that the surface layers are 'shock heated' and obtain high entropy. Those surface layers 'overheated' by shocks are quickly ejected.

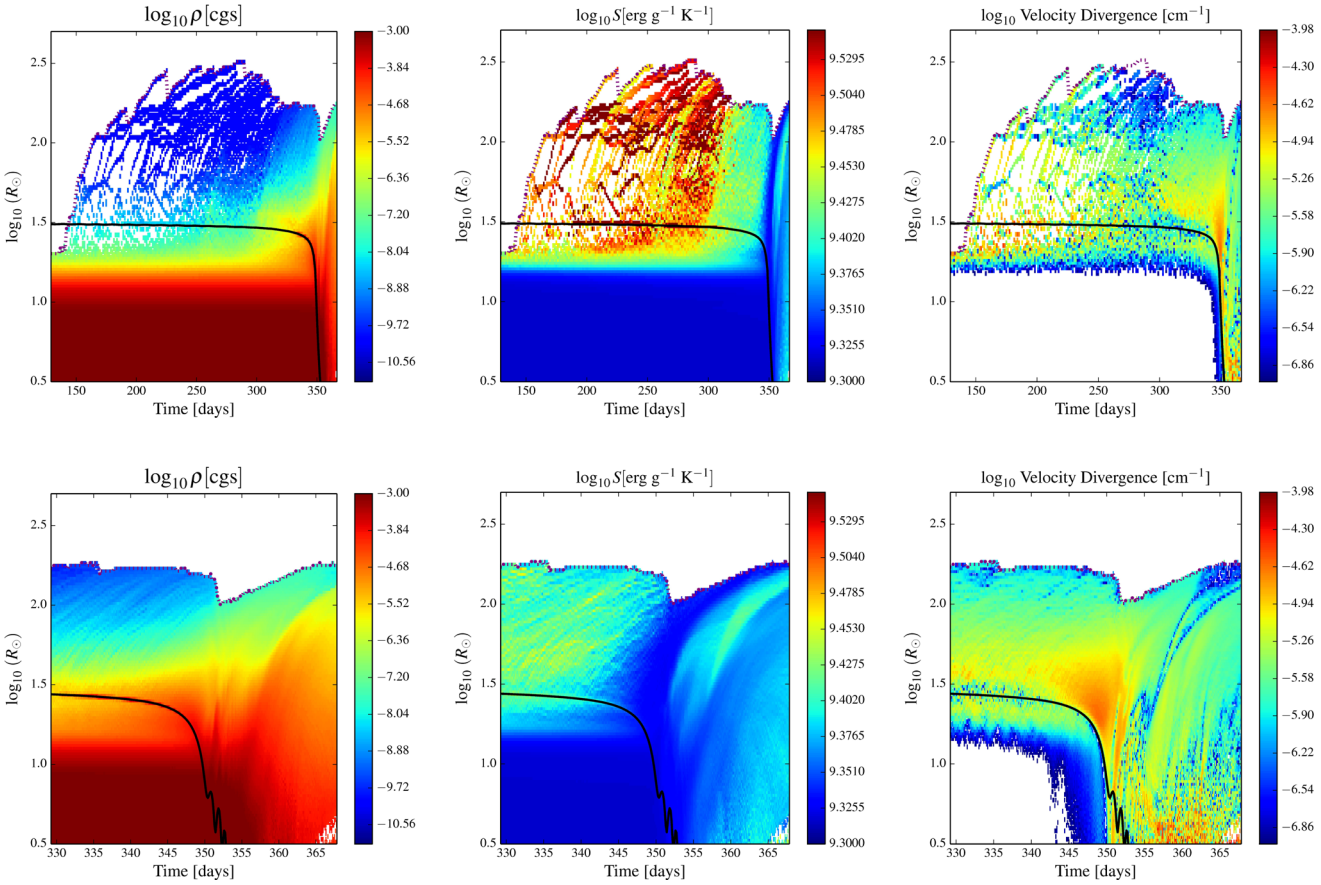

Figure 10. Evolution of the outer layers of the common envelope. We show the case BF36. The figure shows density (left-hand panels), entropy (middle panels) and velocity divergence (right-hand panels), as functions of the radial coordinate. The top panels show long-term evolution, and the bottom panels show a zoom-in to the plunge-in phase. Black solid lines show the location of the companion. The dotted purple lines indicate the surface of the envelope. Note that the plots show only the material that remains bound, not the ejecta.

A similar behaviour continues even while the companion is orbiting inside the envelope, which had expanded to several times its initial size. While the companion is already orbiting inside the envelope (but before the plunge-in), very little of the donor's mass ($\ll$1 per cent) is outside the companion's orbit. Both the entropy generation area and the region with high-velocity divergence propagate inside the orbit, down to the initial donor's radius, but do not affect much of the envelope's mass (this can be seen best in Fig. 10).

The situation changes when more than 1 per cent of the donor's mass surrounds the orbit, and the companion plunges inside the layers that were not shocked previously. Rapid plunge-in takes place, and the entropy is mainly generated outside the orbit. The material with high entropy and high angular momentum becomes quickly unbound, leaves the envelope, and cannot any longer be seen in Figs 9 and 10.

During the slow spiral-in phase, we detect entropy generation due to two processes: quick expansion provides shocks once more, and some entropy possibly comes from the flattening of the rotational profile. As a result, the entropy is increased in the internal part of the envelope, while in the outer part of the envelope, the entropy is almost unchanged (see Fig. 9, where this entropy generation can be seen during the two episodes of mass ejection at the top panel showing the long-term evolution of SS15). This entropy generation can appear to be similar to what was described above as an 'entropy bubble' observed in the past 1D studies. It is noteworthy, however, that the entropy is increased inside this bubble only by about 30 per cent as compared to its initial value. This is much less than predicted by 1D simulations (a factor of several times). The importance of this lack of entropy generation in 3D as compared to 1D will be shown in Section 7.

7 THE ROLE OF THE RECOMBINATION IN DRIVING THE CE EJECTION

The specific energy that is released due to recombination of hydrogen and helium, in the case that they were initially fully ionized, is

$$\varepsilon_{\rm rec} \approx 1.3 \times 10^{13} {\rm erg\ g^{-1}} \times (X f_{\rm H\,I} + Y f_{\rm He\,II} + 1.46 Y f_{\rm He\,I}) . \quad (30)$$

Here X is the hydrogen mass fraction, Y is the helium mass fraction, $f_{\rm H\,I}$ is the fraction of hydrogen that becomes neutral, $f_{\rm He\,I}$ is the fraction of helium that becomes neutral, and $f_{\rm He\,II}$ is the fraction of helium that becomes only singly ionized. In the giant star that we have modelled, the envelope during the giant stage has $X = 0.673$ and $Y = 0.306$. In the case of complete recombination, the released energy is $\sim 1.5 \times 10^{13}$ erg g^{-1}. The equation of state that we use in our SPH code also takes into account ionization of other elements. In more details, we use the tabulated equation of state incorporated from MESA (see section 4.2 of Paxton et al. 2011) and implemented as described in (Nandez et al. 2015). This tabulated equation of state includes recombination energy for H, He, C, N, O, Ne, and Mg. The dominant contribution to the total recombination energy comes

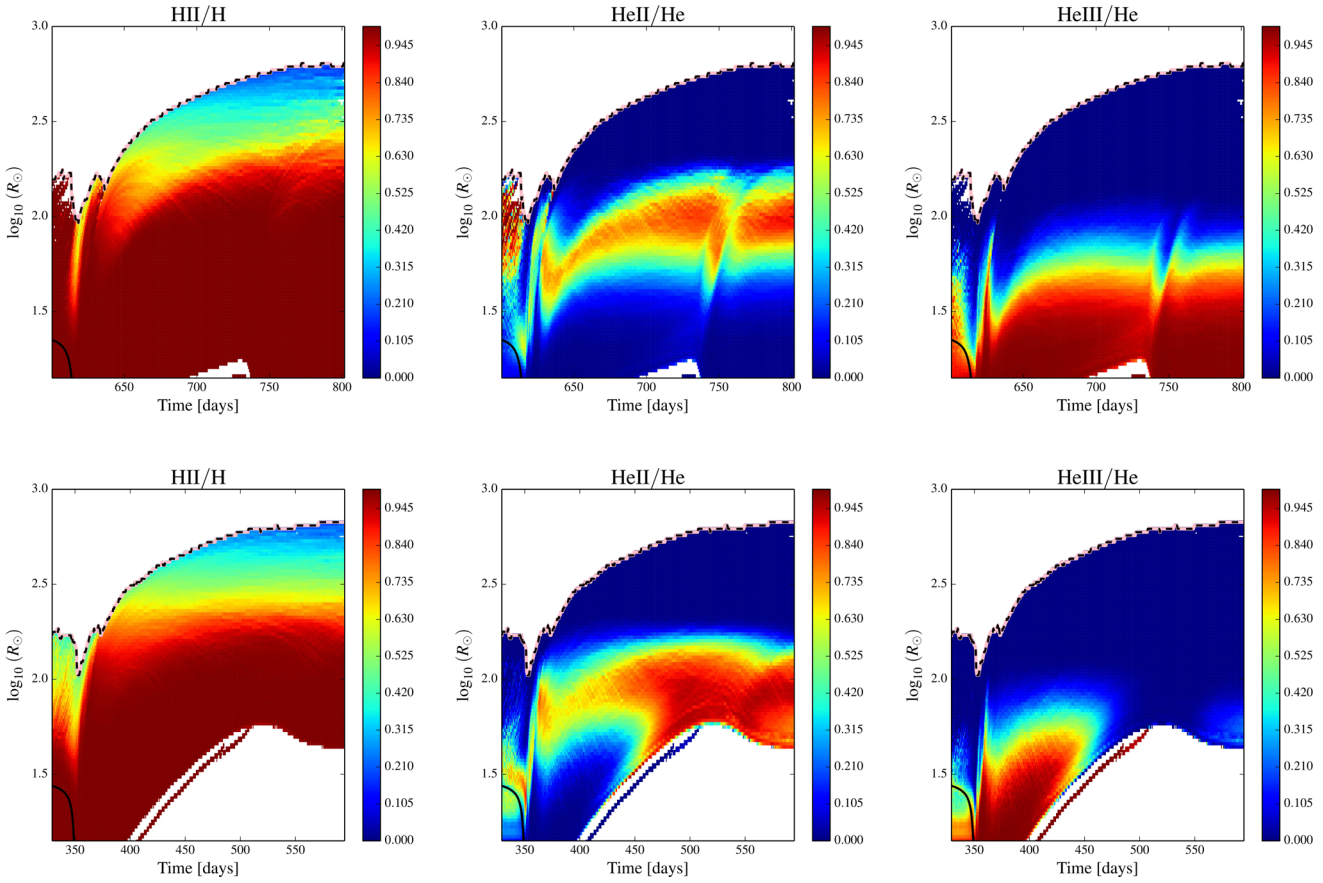

Figure 11. Locations where hydrogen and helium are in different ionization states during the CE evolution. In each panel, the relative fraction of the considered ion is plotted (from 0 to 1.0). We show the cases SS15 (top panels) and BF36 (bottom panels). The plunge-in in the SS15 case ends at about 622 d. During the illustrated evolution, the envelope loses $\sim 0.4\,M_\odot$ (right after the plunge-in). At about 735 d, a shell-triggered ejection takes place (see Section 8). The plunge-in in the BF36 case ends at about 360 d, and during and immediately after this plunge, the envelope loses $0.7\,M_\odot$. After the plunge-in in BF36, the envelope loses $0.4\,M_\odot$ on a longer time-scale. Black solid lines indicate the location of the companion. Dashed lines indicate the surface of the envelope.

from hydrogen and helium, and the other elements only provide 3 per cent of the total recombination energy. When averaged over the whole envelope, the available specific recombination energy per gram for our donor is $\simeq 1.6 \times 10^{13}$ erg g^{-1}, providing 4.7×10^{46} erg in total.

We can compare the efficiency of this energy release to the specific potential energy of the same matter, assuming that the matter is located at a distance r from a gravitating mass to which it is still bound, $m_{\rm grav}$:

$$\varepsilon_{\rm pot} = -\frac{Gm_{\rm grav}}{r} = -1.9 \times 10^{15} {\rm erg\ g^{-1}}\ \frac{m_{\rm grav}/{\rm M}_\odot}{r/R_\odot}. \quad (31)$$

Next, we use the standard assumption that in a stellar envelope, the binding energy is about half of the potential energy (note that here we use the binding energy in its 1D definition). Comparison of $\varepsilon_{\rm rec}$ and $\varepsilon_{\rm pot}$ shows that if the material is cooled down to the point when it can start recombination, and the material at the same moment is located at $r_{\rm rec} \gtrsim 65\,{\rm R}_\odot \times m_{\rm grav}/{\rm M}_\odot$, then *recombination alone* can eject the material with no other energy sources needed. Note that this radius, depending on $m_{\rm grav}$, is smaller than the radius of evolved stars (e.g. asymptotic giant branch stars), however, the material in the envelope of an evolved star is usually too hot to start the recombination. For the hydrogen recombination alone to trigger the material outflow, $r_{\rm rec,H} \gtrsim 105\,{\rm R}_\odot \times m_{\rm grav}/{\rm M}_\odot$. As more of the envelope matter is lost, the radius at which the recombination can act as an energy source powering the outflow, gets smaller. When the upper layers of the envelope are lost, the internal layers start their expansion towards a new equilibrium. Together, these two effects produce a recombination runaway of the envelope that can take place once the recombination starts (see also Ivanova et al. 2015).

Indeed, let us have a look at the case BF36, where the entire envelope is lost. After the plunge-in, during the slow spiral-in, when the envelope is constantly outflowing, the recombination takes places at about the same radius continuously (see Fig. 11). The inner hollow shell has expanded so much, that there is no double ionized helium left. Hydrogen recombination starts at about $\sim 155\,{\rm R}_\odot$ (this is the radius where 5 per cent of H is recombined), while $r_{\rm rec,H} \lesssim 115\,{\rm R}_\odot$ (and it decreases as the envelope outflows). This case is a clear recombination runaway.

Now let us consider the case SS15. Hydrogen recombination starts a bit lower. For e.g. on day 720, 5 per cent of hydrogen is recombined at $130\,{\rm R}_\odot$. Since the post-plunge-in mass below the hydrogen recombination zone is larger than in the case BF36, we find $r_{\rm rec,H} \sim 160\,{\rm R}_\odot$. Hence, hydrogen recombination is not capable of rapidly ejecting the envelope in this case.

We find the case SS20 to be intermediate; similarly to the case BF36, the recombination is established to take place at the radius above $r_{\rm rec,H}$. However, the mass-loss rate is noticeably lower than the mass-loss rate in the case BF36. It is hard to classify this now as a runaway, as the time-scale to lose the entire envelope is longer than

the dynamical time-scale. We classify this as a steady recombination outflow.

Why, in the case of a more massive companion, does the recombination start at a larger radius? In the case of a more massive companion, deeper, initially hotter envelope layers gain the energy to expand enough to start recombination. For e.g. in the SS15 case, the immediate post-plunge-in expansion leads to helium recombination starting at the 0.8 $M_\odot$ mass coordinate, while in the BF36 case, it reached down to 0.45 $M_\odot$. In the latter case, the disturbed layers were initially hotter, and hence this material had to expand to larger distances before it was cold enough to recombine.

We can consider adiabatic expansion of gas that initially had some specific potential energy and specific internal energy, when some (specific) energy is added to the gas. The sum of these energies is the boosted total specific energy of the gas. The layer will start expanding, to find itself at a new 'equilibrium' radius $R_{\rm eq}$, where its total energy, assuming that the gas is not moving, is the sum of its new potential energy and new internal energy, and is equal to the boosted total specific energy of the gas at its old location. In that new location, the gas will have $T(r)/T_0 \approx (R_0/R_{\rm eq})^2$, where T_0 is the gas temperature before the expansion, and R_0 is the location of the gas before the expansion.

Now it can be seen why the difference in the entropy generation between 3D and 1D models, found in Section 6, plays a role in the outcomes. In the case when mechanical energy is added, as in 3D simulations, T_0 is the initial temperature of the (almost) unperturbed star. In the case when the energy is added to the internal energy in the form of heat (resulting in a substantially larger entropy increase in the shared envelope), as in 1D simulations, T_0 is increased compared to the initial temperature of the same layer in the same unperturbed star.

Let us compare the effect of adding the energy mechanically, or as heat, on a specific example – the 1D profile of the star that was used to create our giant in the 3D CEE study presented here. To each mass mesh point in this 1D profile, we add the same amount of energy via the two ways described, and find the temperature when the mass shell reaches its equilibrium radius. Indeed, we find numerically that the second case (where the energy is added as heat) results in a smaller equilibrium radius than the first case (where mechanical energy is added). Adding heat energy also results in matter having a hotter temperature when it reaches the equilibrium radius. When we compare the temperature of two mass shells that have reached the same equilibrium radius after the energy was added, we find that in the added heat energy case, the temperature at the equilibrium radius is also hotter. While no deterministic conclusion can be made on the trend for all possible cases, it is clear that when the energy is added directly to the internal energy, the radius at which the recombinations will start is different.

8 THE EJECTA

In our simulations, we distinguish four types of ejection processes.

(1) '*Initial ejection*' of the outer layers of the original envelope, $\delta M_{\rm ej}^{\rm start}$. This low-mass ejection process takes place before the plunge-in starts, and is seen in all simulated CEEs. A hint of this initial low-mass ejection is suggested from the evolution of the expanding outer layers of the envelope (prior to the start of the plunge-in at about 350 d) shown in Fig. 10.

Ivanova et al. (2013b) have argued, based on the V1309 Sco merger, that the ejecta that accompanies a merger can be estimated by comparing the orbital energy release $\delta E_{\rm orb}(r)$ with the local binding energy of the envelope $\delta E_{\rm bind,env1D}(r)$. Indeed, we observe that in all of our simulations, the orbital energy does not influence the envelope inside the orbit. This supports the idea that the orbital energy release can be compared with the binding energy of the material during the spiral-in, and not only at the final orbit.

The initial low-mass ejection, $\delta M_{\rm ej}^{\rm start}$, can then be found by using

$$\delta E_{\rm orb}(r) + \delta E_{\rm bind,env1D}(r) = 0. \quad (32)$$

From the estimates that use the binding energy profile of the unperturbed star, we find that the expected $\delta M_{\rm ej}^{\rm start}$ is 0.010, 0.022, 0.034, 0.047, and 0.090 $M_\odot$, in cases for companion masses of 0.05, 0.1, 0.15, 0.2, and 0.36 $M_\odot$, respectively. In 3D simulations using the same companion masses, we find that $\delta M_{\rm ej}^{\rm start}$ is 0.01, 0.02, 0.03, 0.045, and 0.1 $M_\odot$. Therefore, equation (32) provides a good method for estimating $\delta M_{\rm ej}^{\rm start}$. However, this is the least massive ejection process, even in cases of mergers.

(2) '*Plunge-in ejection*' of the envelope, $\delta M_{\rm ej}^{\rm plunge}$. This ejection process takes place at the end of the fast plunge-in, when the circumbinary envelope has just formed and the fast orbit depletion has ended. Like the 'Initial ejection', it takes place in all of our simulated CEEs. An example can be seen in Fig. 9: this is when the mass of the envelope is sharply decreasing to 1.4 $M_\odot$, on the time-scale of only a few days. The process of the ejection can also be observed in Fig. 10 for the case BF36, where it takes place after the plunge-in starts (approximately between 355 and 365 d).

This ejection process is likely powered by the mechanical energy that the envelope has absorbed by the time that the orbit has become decoupled from the envelope. We did not find a good method to predict the associated energy release given the initial energy profile. For $\delta M_{\rm ej}^{\rm plunge} + \delta M_{\rm ej}^{\rm start}$, we find from the 3D simulations that 0.03, 0.3, 0.43, 0.53, and 0.75 $M_\odot$ were ejected, for companion masses of 0.05, 0.1, 0.15, 0.2 and 0.36 $M_\odot$, respectively. In the case of BF36, half of the initial envelope was ejected during this stage. It is about the same fraction as was found in the simulations that were performed without recombination energy taken into account (about 40 per cent in Nandez et al. 2015 and about 25 per cent in Ricker & Taam 2012). We cannot rule out however that the inclusion of the recombination might have *enhanced* the plunge-in ejection, as in the case BF36 it led to 50 % of the envelope being ejected during this stage.

(3) '*Recombination runaway*' is the process that led to the complete envelope ejection in the case BF36 (as well as in all of the CEE simulations presented in Nandez & Ivanova 2016). It takes place when the post-plunge-in envelope has cooled down sufficiently to start hydrogen recombination, while at the same time the envelope size has expanded beyond $r_{\rm rec,H}$ (see more details in Section 7). We find that in SS20 and SS15 models, this process does not start promptly after the plunge-in has occurred, and that the material is ejected at a slower rate during this process than in the case of the BF36 case (see Fig. 11). Therefore, for these cases, this process can be thought of as a 'steady recombination outflow'. The average mass-loss rates of these outflows are 2, 0.25, and 0.15 $M_\odot$ per year, for BF36, SS20 and SS15 models, respectively (the dynamical time-scale of the expanded envelope is about a year). In the case of BF36, the recombination driven outflow slowed down to about 0.4 $M_\odot$ per year at about 200 d after the plunge-in.

(4) '*Shell-triggered ejection*' is the sudden ejection of a substantial part of the envelope during the slow spiral-in. This process takes place about one dynamical time-scale of the expanded envelope after the plunge-in process has ended. This phenomenon can be seen for the case SS15 at about 735 d (Figs 9 and 11).

This ejection process is partially powered by the energy release from the recollapsing hollow shell, and partially powered by the triggered recombination. Recall that this hollow shell is bound after the plunge-in, and while it initially expands, it starts to recollapse on its dynamical time-scale. This recollapse results in redistribution of the energy in the envelope, where the contracting shell provides energy for the outer layers, shedding away part of these layers. It is not clear at the moment what total fraction of the envelope this process can eventually remove. First, this process is accompanied with a steady recombination outflow, making it difficult to disentangle the two processes. Secondly, while this process is continuous, it is very slow (even slower than the outflow in the case of the SS20 model), and thus the model becomes a self-regulated spiral-in. Thirdly, we cannot yet compute the contraction of this shell all the way to the binary orbit; thus, we cannot see if this process can extract more energy from the binary and produce several similar re-expansions. In the latter case, no self-regulated spiral-in situation can be expected. We find, however, that the first episode of the shell-triggered ejection takes away almost all of the angular momentum that was remaining in the CE, leaving the CE with less than 0.02 per cent of its initial angular momentum. In addition, the envelope that remains after the shell-triggered ejection is only *marginally* bound – its binding energy is 3×10^{44} erg. If there are no bouncing re-expansions, steady recombination outflow can eject the remaining envelope.

This shell-triggered process does not always happen even for the same initial binary. We ran the initial SS15 binary twice, with the different Courant numbers (for gas SPH particles only). In particular, we changed the second Courant number $C_{N,2}$ (defined as described in Lombardi et al. 2006). Both simulations conserved energy and angular momentum extremely well. The larger value for the Courant number $C_{N,2}$ was 0.6 (used in the simulation SS15), and the smaller value was 0.3 (used in the simulation SS15sC). Both values that we used for $C_{N,2}$ are in the recommended range, between 0.1 and 0.6, for the version of the code we use (Lombardi, private communication).

We find that in the run with the smaller Courant number, SS15sC, the prompt ejection does not occur, and the evolution is similar to SS20, just with a bit slower mass-loss rate of the steady recombination-driven outflows. However, we cannot attribute this divergence between the two runs purely to a numerical error. We traced the difference in the outcomes to the differences in the properties of the SPH particles that are currently in the hollow shell, where those properties were acquired during the plunge-in interaction with the special particles that represent the binary. In the SS15sC case, a fraction of SPH particles in the inner region of the hollow shell have acquired a higher entropy, likely due to more shocks they have experienced. These particles have a higher internal energy, and a higher total energy if compared to SPH particles located at a similar distance from the binary in the SS15 case. The total energy of SPH particles in the shell is about the same, but the distribution of the energies between the particles is slightly different, and in a wider range than in the case SS15. We cannot determine one of the energy distributions between the shell particles as to be more proper than the other.

The natural expectation for SS15sC high-energy particles is that their 'fallback' will start when the shell expands more that in the case SS15. However, while the shell was still expanding (beyond the distance it had maximally expanded in the case SS15), the material starts He recombination (from the double-ionized state to the single-ionized state). This recombination gives an additional energy boost to the hollow shell particles, and prevents its fallback, at least for the duration of the simulation we obtained for SS15sC (for 40 d after the fallback had started in the case SS15). A small deviation in the energy for a fraction of SPH particles in the hollow shell have resulted in a qualitative change of the envelope ejection picture. This indicates that even during the established steady recombination outflow, a CE is recombinationally dynamically unstable with respect to its inner shell recollapse. The condition to prevent this dynamical instability seems to start the fallback after Helium started its recombination. As a confirmation, we find that a weak version of this instability takes place in all the models at the moment when the inner shell started its fallback. As a weak version, we mean that the envelope changes its mass-loss rate at about the same time when the inner shell contracts or re-expands, but this mass-loss rate change is not nearly as noticeable as in the case of SS15. In all those 'weak' cases, Helium is not doubly ionized in the inner shell at the time of fallback. To answer on whether the strong shell-triggered ejection process is a numerical artefact due to a small number of particles near the core (recalling that the total number of SPH particles in this simulation is 100 000), or is the real physical effect that occurs if the fallback starts before the Helium recombination, a study with significantly more particles is required; this is unfeasible at this time, due to the long computational times needed to model a well-established slow spiral-in (see Section 2, also for a description of the computational time-scales, see Nandez & Ivanova 2016).

We stress in this section that usually under the 'CE ejection' term, only complete ejection – the one that leads to naked binary formation – is considered. Such complete ejection is an implicit assumption of the energy budget formalism. However, it is important, that even when a CEE fails to eject the entire envelope, a significant fraction of the mass of the envelope is lost during plunge-in ($\delta M_{\rm ej}^{\rm plunge}$), and that during the slow spiral-in, the CE mass will decrease further.

9 DISCUSSION

We discussed how to average different quantities obtained in 3D CEE simulations to produce information useful for 1D studies. As could have been expected, we find that the asymmetry of the profiles is extreme during the plunge-in, and is non-negligible during a slow spiral-in. For example, the angle-dependent deviation of thermodynamic quantities at the start of the slow spiral-in can reach 50 per cent. Secondly, the typical assumption of spherical symmetry (i.e. the 'thin-shell' approximation for the companion) underestimates the depth of the potential well near the orbit. Finally, the decoupling of the binary and the envelope during a slow spiral-in, with the formation of a dense hollow shell around the binary, provides challenges for 1D codes (where it would appear as a sharp density inversion).

We reviewed the energy balance and discussed how energy conservation can be treated in 1D codes. We outlined three problems when one tries to keep the energy conserved self-consistently in 1D, and provided the energy conservation equation that can be used in 1D codes during a slow spiral-in, once the post-plunge-in configuration is known.

We find that most of the angular momentum is quickly lost from the CE system with the ejecta. In our simulations, there is no corotation between the binary and any part of the CE during any phase of a CEE. In some cases, after the hollow shell formation, only a few particles could have been left within an RL of either the core or the companion; only these particles can be considered as having been in 'corotation'. During a slow spiral-in, the angular velocity becomes constant in most (by mass) of the CE, the spherical symmetry

approximation works well, and the value of the angular velocity is significantly smaller than the local Keplerian velocity anywhere in the envelope.

The flat profile for the angular velocity we derive from our 3D simulations differs strongly from the results of typical 1D CE evolution. In the latter, the region around the binary is always in corotation, as well as a region inside the binary orbit. The angular velocity is then obtained with the diffusion equation, and is found to decrease steadily with the distance from the binary (e.g. Taam et al. 1978; Meyer & Meyer-Hofmeister 1979; Ivanova 2002, note, however, that this was in part by the design of the chosen prescriptions in the 1D codes). It can be argued that the difference between the 3D and 1D profiles may arise from the different ways that viscosity is treated in the two approaches. It is hard to evaluate how well artificial viscosity in SPH matches the convective viscosity (e.g. see discussion in Nandez et al. 2014). It is clear, however, that 3D SPH simulations, when compared to 1D studies, at the same time, are less efficient in transferring angular momentum to the regions near the orbit, and are more efficient in the distribution of the angular momentum throughout the envelope. Therefore, neither too low, nor too high artificial viscosity in SPH, as compared to what is taken as viscosity in 1D simulations, can work as an explanation of these profile differences. In addition, the significant loss of angular momentum with the ejecta does not lead to as significant a spin-up of the envelope as 1D codes predict. Frictional heating from the differential rotation is therefore not expected for most of the envelope, except during the start of the slow spiral-in, when the angular velocity profile quickly flattens.

In addition, the evolution of the entropy of the CE material differs between 3D simulations and 1D results. In 3D, there is no entropy generation within the orbit during the plunge-in. While we can see entropy generation near the surface and a small 'entropy bubble' formation, the entropy increase is much smaller than what 1D studies predict – 3D simulations predict a 30 per cent increase, while 1D results predict a factor of a several increase. In 1D, the entropy is generated because the energy was added as heat.

We have identified four types of ejection processes: the initial ejection, the plunge-in outflow, the recombination runaway outflow, and the shell-triggered ejection. The initial ejection and the plunge-in ejection take place in all the CEEs we have considered, including those that end up with a merger. We provide a simple way to find the mass of the initial ejecta. The prompt plunge-in ejection carries away substantially more mass, but there is no easy way to estimate the magnitude of this ejection. The shell-triggered ejection takes place during the slow spiral-in and is caused by the hollow shell fallback; this provides another prompt ejection process as part of the CE. The recombination runaway outflow starts during a slow spiral-in, once the expanded envelope is cooled down to start hydrogen recombination above $r_{\rm rec,H}$. In this case, the rest of the envelope can be removed within several dynamical time-scales of the expanded envelope. Since the radius at which the recombination energy release overcomes the potential well depends on the entropy of the material, the entropy generation observed in 1D codes will likely predict different outcomes of 1D CE evolution. The combination of a difference in the entropy profile and the entropy's effect on recombination runaway was likely the reason why recombination runaway found in recent simplified 1D studies of CEEs (Ivanova et al. 2015) have happened in models where either a lot of heat was added to the entire envelope, or less heat was added, but in a region that was more confined to the bottom of the envelope (thus keeping the upper envelope's entropy unchanged).

The slow time-scales of recombination runaway can be up to several hundred days, and are getting longer as the mass of the companion decreases. For these cases, 3D simulations are no longer self-consistent, as this is a time-scale on which radiative losses can become important, and hence 1D codes must be used. Note that the envelope is not stationary at any moment, and instead exhibits 'stationary' outflows. Similar recombination-driven outflows were considered for the case of simplified hydrogen envelopes (Bisnovatyi-Kogan & Lamzin 1976), where several possible modes of instabilities were discussed. A recent study of simplified CEE in 1D has shown that the CE is prone to dynamical instabilities (Ivanova et al. 2015), and a runaway recombination was found, but a connection to steady recombination outflows was not made then. The energetic consequences for CEE outcomes in the case of a stationary outflow, instead of a prompt dynamical ejection, were discussed in Ivanova & Chaichenets (2011), but, further studies of the instabilities of envelopes with steady outflows powered by recombination are highly needed.

Using the tools developed for this paper, we inspected the models presented in Nandez & Ivanova (2016), where all of the modelled CEEs resulted in binary formation. There, the models were only analysed for their final states – binaries parameters and energy taken away by the ejected mass. We find that the length of the envelope removal via recombination runaway is increasing with the potential well of the donor. The donor that we consider now had the longest envelope removal time (700 d) out of all the models considered in Nandez & Ivanova (2016) (the next longest time-scale of 250 d occurred in a model that used a $1.6\,{\rm M}_{\odot}$ red giant with a $0.32\,{\rm M}_{\odot}$ core). In this study, we find that the ejection time-scale increases as the companion mass decreases. This implies that the model that provides the time-scales and plateau luminosities of the Luminous Red Novae powered by CEEs (as proposed in Ivanova et al. 2013b), in its future developments, should take into account CEE recombination runaway features, such as the initial envelope binding energy and the mass ratio of the companions.

For a proper treatment of a self-regulated spiral-in, one needs to know the orbit at which the companion slowed down its fall, the mass that remained in the envelope after the companion's plunge, how much angular momentum remained in the envelope, and how much energy was carried away by the ejecta. This can be done only in conjunction with the preliminary 3D simulations that are performed until at least the end of the plunge-in. For the cases when it is not possible, we outline several important points.

(i) The plunge-in takes place on a time-scale comparable to a freefall time-scale. No energy conservation during the plunge can be properly treated in 1D. Instead, a CE structure should be constructed assuming almost adiabatic envelope expansion as a result of the plunge.

(ii) No heat should be added to the envelope – we stress that it is important to produce an adiabatic envelope expansion. Despite changing the energy of the envelope by the same amount when the heat is added, or when the mechanical energy is added, the change of the CE material after these two ways to add energy alters which envelope layers would start recombination. We strongly recommend the use of kinetic energy injection instead of heat injection.

(iii) An effort should be given to model a hollow shell outside of the inner binary in 1D.

(iv) The envelope unavoidably loses a substantial fraction of its mass. While the minimum (initial) ejecta can already be estimated, future studies are needed to determine how to estimate mass involved in the plunge-in ejection.

(v) The expanded envelope should be checked for the condition of recombination runaway, as in this case, no long-term self-regulated spiral-in can take place. All 1D codes should be prepared to detect and treat steady outflows.

(vi) Since most of the angular momentum is lost with the ejected material, the magnitude of the angular velocity in the envelope is likely to be very low. Hence it is rather insignificant to affect either internal structure or provide frictional heating.

In this study, we only considered the specific case of a CEE where the donor star is a low-mass giant, and all the conclusions are made for this case of the donor. While we may expect that the characteristic behaviours we found will also occur in CEEs with more massive donors, future studies and comparisons of 3D simulations with 1D studies using other donors, especially more massive donors, are highly needed.

ACKNOWLEDGEMENTS

NI thanks NSERC Discovery and Canada Research Chairs Program. JLAN acknowledges CONACyT for its support. The authors thank their colleagues, C. Heinke, S. Morsink, E. Rosolowsky, and G. Sivakoff for checking the English in the manuscript. We thank an unknown referee for a number of helpful remarks that helped to improve the manuscript. Computations were made on the supercomputer Guillimin from McGill University, managed by Calcul Québec and Compute Canada. The operation of this supercomputer is funded by the Canada Foundation for Innovation (CFI), Ministére de l'Économie, de l'Innovation et des Exportations du Québec (MEIE), RMGA and the Fonds de recherche du Québec – Nature et technologies (FRQ-NT).

REFERENCES

Ahrens J., Geveci B., Law C., 2005, The Visualization Handbook, 717
Antonini F., Lombardi J. C., Jr, Merritt D., 2011, ApJ, 731, 128
Ayachit U., 2015, The ParaView Guide: A Parallel Visualization Application, ParaView 4.3 edition. Kitware, Inc.
Bisnovatyi-Kogan G. S., Lamzin S. A., 1976, Astron. Zh., 53, 742
Church R. P., Dischler J., Davies M. B., Tout C. A., Adams T., Beer M. E., 2009, MNRAS, 395, 1127
Cullen L., Dehnen W., 2010, MNRAS, 408, 669
Davies M. B., Ruffert M., Benz W., Muller E., 1993, A&A, 272, 430
Eggleton P. P., 1971, MNRAS, 151, 351
Eggleton P. P., 1972, MNRAS, 156, 361
Endal A. S., Sofia S., 1976, ApJ, 210, 184
Endal A. S., Sofia S., 1978, ApJ, 220, 279
Gaburov E., Lombardi J. C., Jr, Portegies Zwart S., 2010, MNRAS, 402, 105
Glebbeek E., Pols O. R., Hurley J. R., 2008, A&A, 488, 1007
Hall P. D., 2015, PhD thesis, Univ. Cambridge
Heger A., Langer N., 1998, A&A, 334, 210
Heger A., Langer N., Woosley S. E., 2000, ApJ, 528, 368
Hernquist L., Katz N., 1989, ApJS, 70, 419
Hwang J., Lombardi J. C., Jr, Rasio F. A., Kalogera V., 2015, ApJ, 806, 135
Ivanova N., 2002, PhD thesis, Univ. Oxford
Ivanova N., 2011, ApJ, 730, 76
Ivanova N., Chaichenets S., 2011, ApJ, 731, L36
Ivanova N., Chaichenets S., Fregeau J., Heinke C. O., Lombardi J. C., Woods T. E., 2010, ApJ, 717, 948
Ivanova N. et al., 2013a, A&AR, 21, 59
Ivanova N., Justham S., Avendano Nandez J. L., Lombardi J. C., 2013b, Science, 339, 433
Ivanova N., Justham S., Podsiadlowski P., 2015, MNRAS, 447, 2181
Livio M., Soker N., 1988, ApJ, 329, 764
Lombardi J. C., Jr, Proulx Z. F., Dooley K. L., Theriault E. M., Ivanova N., Rasio F. A., 2006, ApJ, 640, 441
Lombardi J. C., Jr, Holtzman W., Dooley K. L., Gearity K., Kalogera V., Rasio F. A., 2011, ApJ, 737, 49
Lopez-Canelas N., Politano M., 2015, IAU General Assembly, 22, 55902
Luan J., Phinney E. S., 2011, AAS/High Energy Astrophysics Division, Vol. 12. Available at: http://adsabs.harvard.edu/abs/2011HEAD...12.0305L
Menon A., Heger A., 2015, IAU General Assembly, 22, 50783
Meyer F., Meyer-Hofmeister E., 1979, A&A, 78, 167
Monaghan J. J., 2002, MNRAS, 335, 843
Nandez J. L. A., Ivanova N., 2016, MNRAS, 460, 3992
Nandez J. L. A., Ivanova N., Lombardi J. C., Jr, 2014, ApJ, 786, 39
Nandez J. L. A., Ivanova N., Lombardi J. C., 2015, MNRAS, 450, L39
Ohlmann S. T., Röpke F. K., Pakmor R., Springel V., 2016, ApJ, 816, L9
Paczynski B., 1976, in Eggleton P., Mitton S., Whelan J., eds, Proc. IAU Symp. 73, Structure and Evolution of Close Binary Systems. Kluwer, Dordrecht, p. 75
Passy J.-C. et al., 2012, ApJ, 744, 52
Paxton B., Bildsten L., Dotter A., Herwig F., Lesaffre P., Timmes F., 2011, ApJS, 192, 3
Paxton B. et al., 2013, ApJS, 208, 4
Perets H. B., Li Z., Lombardi J. C., Jr., Milcarek S. R., Jr., 2016, ApJ, 823, 113
Podsiadlowski P., 2001, in Podsiadlowski P., Rappaport S., King A. R., D'Antona F., Burderi L., eds, ASP Conf. Ser. Vol. 229, Evolution of Binary and Multiple Star Systems. Astron. Soc. Pac., San Francisco, p. 239
Rasio F. A., Livio M., 1996, ApJ, 471, 366
Ricker P. M., Taam R. E., 2012, ApJ, 746, 74
Sandquist E. L., Taam R. E., Chen X., Bodenheimer P., Burkert A., 1998, ApJ, 500, 909
Taam R. E., Bodenheimer P., Ostriker J. P., 1978, ApJ, 222, 269
Webbink R. F., 1975, PhD thesis, Univ. Cambridge
Webbink R. F., 1984, ApJ, 277, 355

APPENDIX A: ANGULAR MOMENTUM IN 3D CODES

The angular momentum of a particle k in SPH is

$$\boldsymbol{L}_k = \boldsymbol{r}_k \times (m_k \boldsymbol{v}_k) = L_{x,k}\hat{x} + L_{y,k}\hat{y} + L_{z,k}\hat{z}, \tag{A1}$$

where the components of the angular momentum for x, y, and z are given by

$$L_{x,k} = m_k(y_k v_{z,k} - z_k v_{y,k}),$$
$$L_{y,k} = m_k(z_k v_{x,k} - x_k v_{z,k}),$$
$$L_{z,k} = m_k(x_k v_{y,k} - y_k v_{x,k}),$$

respectively. The total angular momentum for the system is,

$$\boldsymbol{L} = \sum_k^N \boldsymbol{L}_k, \tag{A2}$$

and its magnitude is

$$L = |\boldsymbol{L}| = \sqrt{L_x^2 + L_y^2 + L_z^2}, \tag{A3}$$

where

$$L_x = \sum_k^N m_k(y_k v_{z,k} - z_k v_{y,k}),$$

$$L_y = \sum_k^N m_k(z_k v_{x,k} - x_k v_{z,k}),$$

$$L_z = \sum_k^N m_k(x_k v_{y,k} - y_k v_{x,k}).$$

The angular momentum (by its components) around a particular point p can be calculated as

$$L^p_{x,k} = m_k \left[(y_k - y^p)(v_{z,k} - v^p_z) - (z_k - z^p)(v_{y,k} - v^p_y)\right],$$

$$L^p_{y,k} = m_k \left[(z_k - z^p)(v_{x,k} - v^p_x) - (x_k - x^p)(v_{z,k} - v^p_z)\right],$$

$$L^p_{z,k} = m_k \left[(x_k - x^p)(v_{y,k} - v^p_y) - (y_k - y^p)(v_{x,k} - v^p_x)\right].$$

This paper has been typeset from a TEX/LATEX file prepared by the author.